October 2008

Design, Build, and Testing of an Aircraft Lasercom Terminal Compact Optical Module (ALT-COM)

Bradley Armand Scoville
Worcester Polytechnic Institute

Steven Philip Rose
Worcester Polytechnic Institute

Massachusetts Institute of Technology
Lincoln Laboratory

Design, Build, and Testing of an Aircraft Lasercom Terminal Compact Optical Module (ALT-COM)

Steven P. Rose
Bradley A. Scoville
Dr. Jeffrey M. Roth
Group 66

16 October 2008

This work was sponsored by the Department of the Air Force under Air Force Contract FA8721-05-C-0002. Opinions, interpretations, conclusions, and recommendations are those of the author and are not necessarily endorsed by the United States Government.

ABSTRACT

This report discusses the design, construction, and testing of a compact, aircraft laser communication terminal developed at the Massachusetts Institute of Technology, Lincoln Laboratory. The project focuses on scaling down an existing experimental terminal in both size and weight and adding new functionalities. The final design is an initial effort to transition from laboratory-grade hardware to a path-to-flight design.

EXECUTIVE SUMMARY

The purpose of this project is to design, construct, and test a Aircraft Lasercom Terminal Compact Optical Module (ALT-COM) with the Massachusetts Institute of Technology, Lincoln Laboratory. The Advanced Lasercom Systems and Operations Group has developed a Tracking Testbed for experimental testing of pointing, acquisition, and tracking of a lasercom link between spacecraft and aircraft.

The Tracking Testbed consists of three components: the aircraft terminal, spacecraft terminal and an emulator that simulates the effects of environmental disturbances in an air-to-space link. These disturbances include platform jitter, atmospheric scintillations, and boundary layer distortions. This project focuses on scaling down the experimental aircraft terminal in both size and weight in an initial effort to transition from laboratory-grade hardware to path-to-flight design. In addition to reducing the size of the terminal, new functionalities have been added including a beacon generation system.

The final design of ALT-COM was mounted on a 12×18 in optical breadboard, a 75% size reduction from the Tracking Testbed aircraft terminal. The initial design was laid out to fit on a smaller board, however due to the time constraints of the project, the size of the board was increased by the quad-cell (QC) mount that was readily available in the lab. Future efforts can be focused on obtaining a smaller quad-cell mount to additionally reduce the size of ALT-COM.

ALT-COM consists of one transmit fiber launch assembly (Tx FLA), as opposed to two separate Tx FLA used in the existing Tracking Testbed aircraft terminal. The lens, mounted on the piezoelectric stage, is moved between two discrete locations to control the divergence of Tx beam. The beacon beam, used during acquisition of an air-to-space link, is selected by moving the stage 400 μm. At the 0 μm position the communication beam is selected. This beam is used for high data rate communication after the link has been acquired. The beacon generation system performance was investigated to find an average switching speed of 9.37 ± 0.77 ms. This satisfies our requirement of switching speed less than 50 ms.

The divergence of the beams was measured with a wavefront sensor (WFS). This divergence had to be minimized for the communication signal in order to keep the beam narrow across long distances. This helps to maximize operating efficiency and maintain high data rates. Conversely, the beacon signal is required to have a large divergence to allow for quick link acquisitions. From the final component in ALT-COM, the divergences were measured to be 0.579 mrad ($1/e^2$) for communications, and 3.02 mrad ($1/e^2$) for beacon.

A new piezoelectric fast-steering mirror was characterized with a 25-mm diameter mirror. The mirror has roughly 1600 μrad of mechanical angular range (throw) with a control input between 0 V and 8 V for both azimuth and elevation axes. A control voltage of 4 V was applied to bias both axes during beam alignment to allow maximum angular movement. Frequency response measurements, taken with a dynamic signal analyzer (DSA), show a bandwidth close to 200 Hz for the FSM, with

attenuation at approximately 5 dB per decade after this frequency. The FSM used in the Tracking Testbed has a bandwidth close to 1 kHz. The new FSM bandwidth is much smaller in comparison, however it was still used in ALT-COM to test its performance in a tracking system with a quad-cell detector.

After mounting the quad-cell head and closing the feedback loop between the FSM and QC, the tracking feedback loop (TFL) was characterized. This was done by finding the frequency response of the gimbal tracking interface and summing the logarithmic magnitude and phase response plots with those of the FSM. This yielded the frequency response of the feedback loop. With a unity gain integrator in the gimbal tracking interface, the bandwidth of the loop was initially 20 Hz. After analyzing the phase margin of the loop it was determined that the bandwidth could be increased to a few-hundred Hertz without affecting the stability of the system. Therefore the gain of the integrator was changed to 10 to increase the bandwidth to 200 Hz. A rejection frequency plot was obtained in order to verify the response's cutoff frequency.

The last test on the tracking feedback loop was to assess performance of the loop with platform jitter. Platform jitter was applied, by control to the PAM, according to three beam jitter models. The test was run for 0.5, 1.5, and 4 in beam platform jitter models. The DSA was used to determine the power spectral density of the applied jitter and residual jitter from the output of the quad-cell controller. The resulting PSD graphs were integrated to find the applied and residual jitter in microradians. The TFL was successful in reducing platform jitter for both 0.5- and 1.5-in beam models. In particular, for the 1.5 in beam model, applied jitter 250% of the beamwidth was reduced to 25% of the beamwidth. For the 4 in test the TFL was less effective in removing platform jitter for the Az axis. Additional tests revealed the FSM throw (angular dynamic range) in the Az axis was the limitation for the 4 in beam platform jitter test.

Optical power losses were measured throughout the terminal and documented as part of a link budget. Link budget calculations help to indicate overall loss associated with communication, as well as identify losses due to individual components and channels. This allows characterization of the current terminal, as well as to identify future improvements. The current link budget suggests a 2.5 Gb/s link could be maintained by ALT-COM with high-altitude aircraft. This link would require a power of 40 dBm (10 W), and would have an error margin of 0.47 dB for reception and 2.89 dB for transmission from ALT-COM.

In conclusion, this project is successful in making an initial transition from laboratory-grade hardware to path-to-flight design. The ALT-COM terminal is 25% of the size of the Tracking Testbed aircraft terminal. The new fast-steering mirror has less dynamic range and bandwidth of the Tracking Testbed FSM, however is effective in the TFL for lower bandwidth applications. The ALT-COM TFL was successful in removing platform jitter for both 0.5- and 1.5-in beam models.

ACKNOWLEDGMENTS

We wish to acknowledge Tim Williams, Bob Murphy, Bill Wilcox, Dave Crucioli and Worcester Polytechnic Institute Professors William Michalson and Germano Iannachionne for their helpful guidance on this work.

TABLE OF CONTENTS

LIST OF ILLUSTRATIONS

LIST OF TABLES

1. INTRODUCTION

The Tracking Testbed (TTB) is an experimental arrangement designed by MIT Lincoln Laboratory Advanced Lasercom Systems and Operations Group to emulate laser communications (lasercom) between aircrafts and spacecrafts. There are three major components: the aircraft terminal, the spacecraft terminal, and an emulated channel to simulate environmental disturbances such as platform jitter, atmospheric scintillations, and boundary layer distortions.

The Testbed's current aircraft terminal is not modular and occupies a large size (24 x 36 in). The driving motivation of this project was to reduce the size and weight of the aircraft terminal, to add new functionalities, and to investigate the use of new hardware that supports a smaller footprint. The smaller terminal provides an initial transition to path-to-flight design. It also permits integration of it into the Coarse-Pointing Motion Emulator, a large two-axis yoke that can evaluate beam director pointing performance under large-angle aircraft maneuvers. The goal of this project was to design and build the Aircraft Lasercom Terminal Compact Optical Module (ALT-COM).

In order to create a smaller, more compact module, redundant components have been removed from the terminal. As opposed to the current transmit fiber launch assembly (FLA), which includes a separate laser for both the beacon and communication beams, one laser was used for both transmit modes. A piezoelectric stage was used to control the distance of the lens from the laser, changing the divergence of the beam. This technique allows the same FLA hardware to generate both a narrow, communications beam and a broad, beacon beam.

The existing tracking control loop includes both a camera and quad-cell. These devices provide feedback on the position of the beam to the fast-steering mirror (FSM) which tracks the incoming optical beam. For ALT-COM, we use only a FSM and QC for tracking, and do not currently include a camera.

Throughout the building stages, the wavefront error, beam size, and insertion loss were monitored at several locations. The beacon-to-communication switching speed and range was evaluated along with the beam divergence for the acquisition beacon. A new FSM was evaluated for steering range and bandwidth. Finally, a compact PAM was verified to operate in a manner suitable for this application.

With the addition of new hardware, and removal of redundant components, the components of ALT-COM had to be properly interfaced. This effort included programming new control software for existing components, and modification of software for existing components. For proper connections between components in ALT-COM, the control signals needed conditioning through analog circuitry.

The design structure of ALT-COM was first explored with AutoCAD. This aided in limiting potential errors due to actual limits in component placement. Control software was developed in parallel with component installation. Optical alignment, testing, and documentation were performed as components were installed and the control software was created. MIT Lincoln Laboratory Advanced Lasercom Systems and Operations Group sponsored this project with Dr. Jeffrey M.

Roth as the project supervisor. At the conclusion of the project the ALT-COM design and operating conditions were presented in a summative final presentation to the members of the Advanced Lasercom Systems and Operations Group, as well as the community of MIT Lincoln Laboratory. Lincoln Laboratory will retain documents of work and the final product for use as reference or further experimentation.

2. BACKGROUND

This section provides background information necessary to understand the motivation and procedures of the ALT-COM project. First, optical communications will be introduced in relation to other methods of communication. Second, free space optics, in particular laser communication, will be presented along with the challenges of creating a link between aircraft and spacecraft. We will then provide information on the research that MIT Lincoln Laboratory has done to emulate an air-to-space link and the existing work on a Compact Lasercom Terminal. Finally, we will discuss some of the optical and electrical components, as well as the testing equipment used for construction of ALT-COM.

2.1 COMMUNICATION MEDIA

Communications signals may be transmitted through a variety of media. Copper wire, a widespread medium, has been used to network homes and businesses since the establishment of POTS (Plain-old Telephone Service). In the early days of the Internet, the existing POTS infrastructure was used to network computers. As computer networks expanded, a higher demand for bandwidth occurred. Copper-wire-based POTS infrastructure could no longer meet the demand. In order to satisfy the growing bandwidth requirements, other communication media were introduced to relieve the strain on the POTS infrastructure.

Efforts were focused on higher bandwidth wired media as well as wireless media. Fiber optics technology was investigated as an addition to the wired networks. Higher carrier frequencies allowed for a great amount of bandwidth and throughput. However, regardless of the reliability produced, higher deployment costs and longer deployment times limited the use of fiber optics. In 2002, it was noted that only 5% of commercial businesses were connected to a fiber backbone, although 75% were within 1 mile of such a backbone. Despite the limited use of optical fiber in residential networks, this technology has met bandwidth demands circa 1995 to 2008 [12].

Radio-frequency (RF) has been an established wireless technology that has carried modulated signals. RF has been especially useful in providing mobile communication through radio, cellphones, and satellites. For mobile communication, development emphasized transmission distance, as well as capability for quick creation of network links as users move in and out of range. The implementation of RF transmission has been modified to support higher bandwidth requirements. Techniques include more reliable modulation schemes as well as antenna design and placement. RF-based networks have the capability of providing long distance coverage, however the channel capacity is limited and spectrum licenses are costly.

Optical communications provides an alternative method of communication that offers significantly higher data rates than Radio Frequency (RF) techniques. Free space optics (FSO) has a number of advantages, including scalable bandwidth, high data rates with compact apertures, rapid deployment (hours vs. months), and high cost effectiveness (at least one-fifth) [12]. Furthermore, since FSO has small beamwidths and broadcasts narrow beams, it is more secure against

eavesdroppers. Also, free space optical communication in the 1.55-μm infrared band is generally unregulated [12].

2.2 AIR-TO-SPACE LASER COMMUNICATIONS

In order for two lasercom terminals to establish a communications link, they must first be pointed towards each other. For terrestrial networks, this is mostly built into the deployment of such networks, with other fine tuning techniques responsible for dealing with disruptions (i.e. building sway). However, in establishing a connection between mobile platforms, this must be handled dynamically and automatically.

An aircraft attempting to send a signal will first need to locate a satellite. This is done by scanning with a beacon signal. The width of the beacon signal is one important factor in determining acquisition time. Figure 1 plots the maximum acquisition time versus azimuthal uncertainty (elevation uncertainty is held constant) for different configurations of transmitted beamwidth, receiver field of view (FOV) [8]. Broader beams and larger receivers are show to work more effectively; however, these will cost addition power to the laser or increase weight on the satellite.

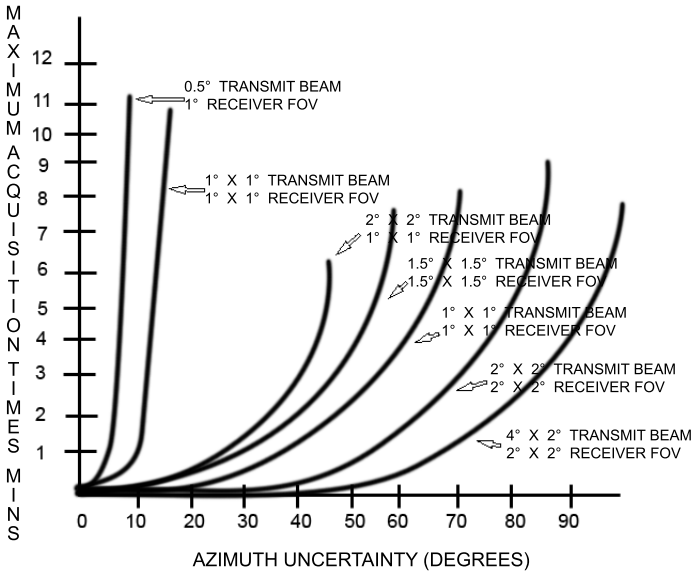

Figure 1. Acquisition time explored. After Ref. [8]

For this reason, one goal is to have a beacon signal with a wide angle of divergence. However, the beam must provide sufficient power density to be detectable at remote terminals. The initial response from the satellite will be such a beam. The link can now be created as the aircraft returns a narrow beam signal and halts beacon scanning. From this point on, the narrow beams will be used for both communicating as well as allowing for both terminals to track each others location [8].

After receiving a response from the spacecraft, the two terminals begin to track each other using the incoming beams as a reference. Stabilizing out any motion of the reference beam in turn removes local platform jitter and allows the terminals to deliver stable power to each other. With the platform jitter removed, the aircraft terminal can then switch to a narrow beam that delivers sufficient power density to support high-rate communications signaling.

2.3 CHALLENGES OF LASERCOM IN AIR-TO-SPACE LINKS

There are particular design challenges to be met for lasercom systems. Environmental conditions can distort the beam in a number of ways. Furthermore, FSO is a line-of-sight technology, therefore two points must be able to see each other if they are to connect and maintain communication. This poses additional challenges when designing systems for moving terminals.

Fog is the major challenge of FSO communication near the Earth's surface. The tiny droplets of water that compose fog can alter light passing through them, or completely hinder passage. This occurs through a combination of absorption, scattering, and reflection. Cloud cover poses the same challenges when Earth-to-space communications are required by FSO. Absorption caused by water removes photons from the beam, which in turn decreases the energy of the beam, causing attenuation. This hampers the availability of the communications link. Absorption occurs more readily at certain wavelengths than others therefore it can be mitigated by the choice of operating wavelength [12].

Scattering and reflection redirect energy flow. This can cause a significant reduction in beam intensity. Of the three types of scattering (Rayleigh, Mie, and nonselective), Mie scattering is the most important to consider in FSO systems. Attenuation caused by Rayleigh scattering (from particles much smaller than the operating wavelength) has a strong inverse proportion to wavelength [2]. By choosing a large wavelength in the infrared band (1550 nm in particular), the effect of Rayleigh scattering is mitigated. However, as the size of the scattering particles reaches near to the wavelength of the beam, Mie scattering becomes a dominant effect that does not have a strong wavelength dependence [2]. Non-selective scattering fills the remaining regime where the scattering particle is much larger than the wavelength. Where non-selectively scattering particles are sufficiently dense, such as in fog and clouds discussed above, they act as an opaque layer between Earth and space [2]. This can be avoided in a mobile air-to-space link by relocating to a clear area or by rising above the cloud cover.

Scintillation is the effect of varying eddies on the wavefront. Different portions of the beam will be affected independently which leads interference at a detector, as well as potentially altering the beam divergence or path. Power will appear to fluctuate due to this interference, and the beam will seem to move erratically [5]. Furthermore, the effects are constantly changing in time, and the path varies as air and space craft move relative to each other and the atmosphere.

Physical obstructions are important due to FSO being a line-of-sight technology. Temporary obstructions (such as birds) only bring short interruptions and can be addressed with multi-beam systems. Permanent obstructions will require redeployment of the terminals. Maintenance of a line-of-sight link requires that motions be accounted for. Loss of line-of-sight could be caused

by building sway, motions of the terminals, or jittering of the terminals (due to motions of the platforms). Additionally, terminals must be able to track the moving positions of each other for applications such as air-to-space laser communications [12].

2.4 MIT LINCOLN LABORATORY TRACKING TESTBED

This section provides information on the Tracking Testbed (TTB) created by MIT Lincoln Laboratory to simulate laser communication in an air-to-space link. We will first discuss the purpose of the TTB, the aircraft and spacecraft terminal configurations, as well as the platform and channel emulator.

2.4.1 Purpose of the Tracking Testbed

The Tracking Testbed was developed by MIT Lincoln Laboratory to create two terminals, one for a spacecraft, one for an aircraft, and establish laser communication between them. More importantly the Testbed was developed to test and characterize the functionality of the laser link with expected conditions in space. Several environmental conditions as well as motion of the aircraft and spacecraft were modeled in the platform and channel emulator. A block diagram of the Tracking Testbed is shown in Figure 2.

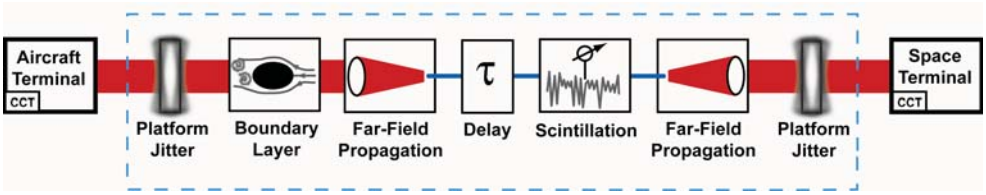

Figure 2. Environment implemented by the Tracking Testbed.

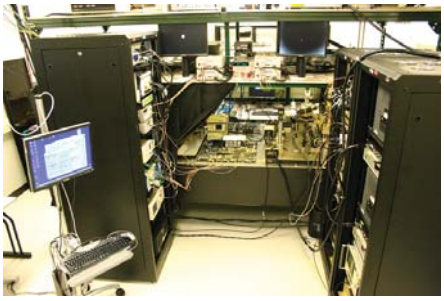

Figure 3. MIT Lincoln Laboratory Tracking Testbed.

2.4.2 Terminal Configuration

The spacecraft and aircraft terminals in the Tracking Testbed share very similar configuration as shown in Figure 5. There are two subsystems in each terminal. The first is the fiber launch assembly (FLA). This includes the transmit FLA and the receive FLA. For the aircraft terminal the Tx FLA includes two lasers in order to generate the beacon and communication beams. The active beam is selected by an optical switch. The Tx FLA for the spacecraft operates in only communication beam mode. For both terminals the Tx beam is directed at a point-ahead mirror (PAM) that reflects the beam such that once the beam travels through the polarization beam splitter (PBS) and fast-steering mirror (FSM) the beam is directed ahead of the mobile, receiving terminal. Figure 4 demonstrates the design concepts of the space and air craft terminals.

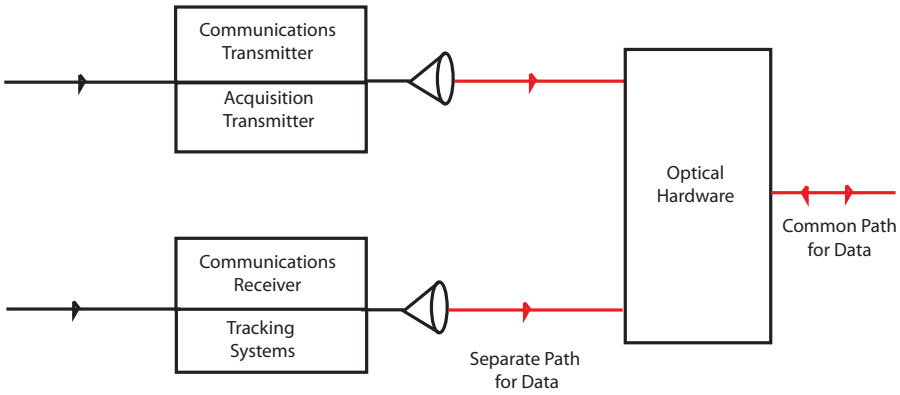

Figure 4. Design concepts of lasercom.

The second subsystem in the terminal is the tracking feedback loop. The FSM is part of this loop. It reflects the incoming laser beam to the PBS which splits it into the Rx fiber through a lens. The FSM is adjusted at the proper angle through a feedback loop with the CamLink and quad-cell (QC). The external board connects the control signals from the CamLink and the QC to the FSM controller.

2.4.3 Platform and Channel Emulator

Between the space and air craft terminals, the Channel Emulator is used to distort the beam. This is done to emulate environmental effects on the beam, similar to those that would be experienced in an air-to-space lasercom system. Furthermore, a time delay is imposed to more accurately synthesize the complications of long-distance communication.

The first impairment the Channel Emulator applies is platform jitter. Both of the craft generally experience small, unpredictable shakes, caused by air turbulence. This distortion is implemented by placing a platform jitter mirror just before each terminal which jitters in a similar manner. Reflected light has slightly altered trajectories depending on the particular position of the

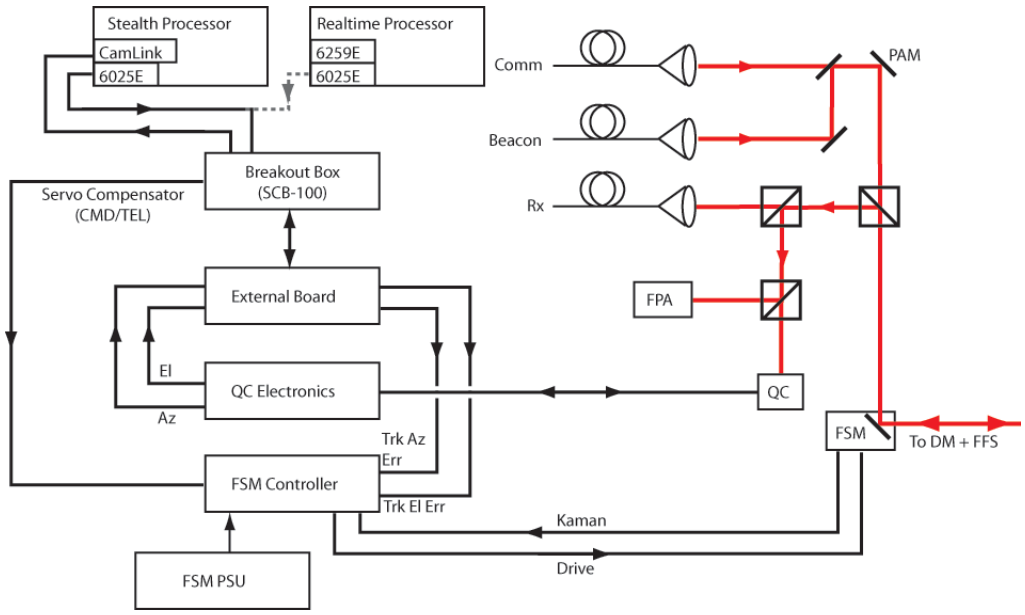

Figure 5. Existing terminal tracker configuration.

mirror is in when struck. Note that this does not account for the slower, wide-angle changes that would be present if the aircraft were to bank left or right.

The next task is to make the signal look like it had come from a long distance. The signals sent have curved wavefronts, but when viewing through a tiny aperture from long distances, they appear almost flat as show in Figure 6.

Lenses have a characteristic focal length, the distance at which an object from the lens appears to be infinitely far away. By placing a lens at its focal length from the laser source, the light is collimated – the wavefronts are nearly flat.

While passing through the fiber, the signal is then re-transmitted after adding delay. A typical round-trip time would be approximately one-quarter of a second. However, before the signal is re-transmitted, it is attenuated to replicate loss caused by passing through Earth's atmosphere.

Finally, boundary-layer impairments are emulated. These impairments are caused by non-laminar air-flow around the aircraft, and are only introduced on the aircraft side of the Channel Emulator. A deformable mirror is used to distort the beam's qualities, as shown in Figure 7. Different distortions are used to account for the directional dependence of the turbulence the beam will encounter.

2.5 COMPACT LASERCOM TERMINAL

In March 2008, Tim Williams, one of the members of the Advanced Lasercom Systems and Operations Groups, started to work on the design of a compact lasercom terminal. The design was

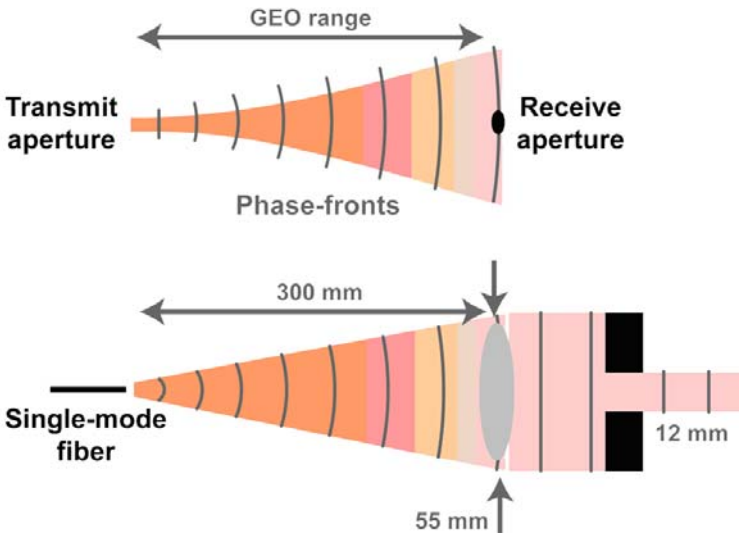

Figure 6. Simulating a long-distance signal with a lens.

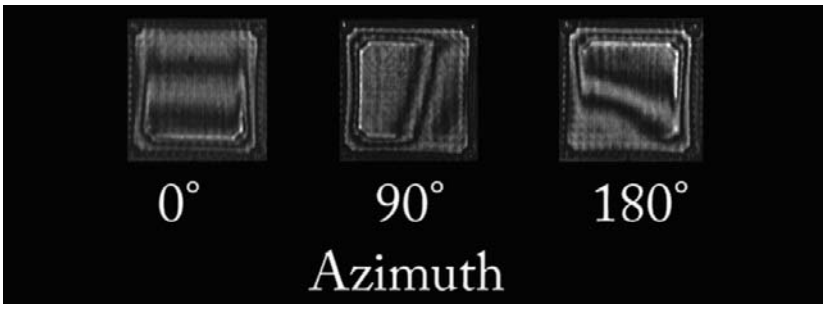

Figure 7. Deformable mirror settings.

fit to requirements for optical and mechanical performance, as well as environmental conditions. The initial design introduced the piezoelectric stage and lens configuration for switching between beacon and communication operations as well as using a fast-steering mirror in place of the point-ahead mirror. The design did not specify a replacement or modification to the current fast-steering mirror, and it retained the focal plane array for target acquisition – both of which are addressed in this revision. The layout of optical components for the compact lasercom terminal was drawn in AutoCAD. The layout is shown in Figure 8 [3].

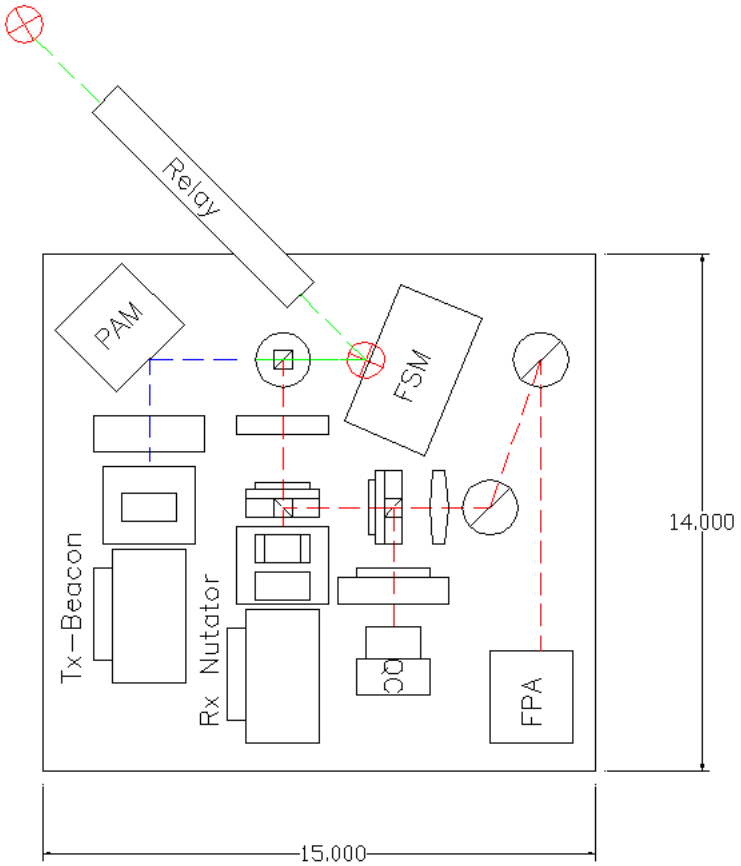

Figure 8. Compact lasercom terminal design by Tim Williams.

2.6 FREE-SPACE OPTICAL COMPONENTS

This section provides background information on both optical and electrical components that are used in the existing aircraft terminal, and the final design of ALT-COM. We will first discuss polarization beam-splitters, then discuss quad-cell detectors and finally an important tool used during construction to verify wavefront properties.

Directional coordinates are taken relative to the beam propagation. This helps to simplify understanding by breaking down Cartesian axis into particular definitions, rather than along a global standard. Figure 9 gives a model of how local coordinates are determined. The beam travels along the Z-axis, which also doubles as the optical axis for each interaction. The Y-axis describes relative heights, and the X-axis left-to-right deviations from the beam, both of which are generally required to be nulled.

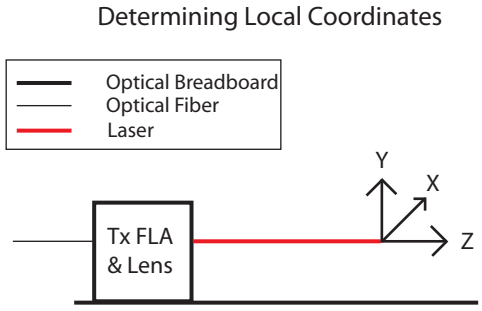

Figure 9. Local coordinates.

2.6.1 Polarization Beam-Splitters

Beam splitters are optical components that are used to separate an incoming light beam into two paths. The incoming light beam is combined with the transmission beam onto a common path using a beam splitter. Beam splitters are typically made of semitransparent metallic or dielectric film on a glass substrate. A special type of beam splitter, called a polarization beam splitter (PBS), is comprised of two cemented prisms of anisotropic crystal in different orientations [7].

Polarization of light refers to the direction in which the electric field oscillates. From Maxwell's equations, these oscillations must be orthogonal to the direction of propagation. In general, all possible polarizations are reconstructed from two orthogonal polarizations, P- and S-polarization. These polarizations are specifically defined only in a plane of incidence, which contains the incident, reflected, and refracted beams from an interface, as shown in Figure 10. P-polarization oscillates in this plane, whereas S-polarization oscillates perpendicularly to it [9]. Since the beam in ALT-COM is to be maintained at a constant height, all interactions should exist in a single plane of interaction which maintains the meaning of these polarizations. It should be noticed from the coordinate definition given in Figure 9 that P-polarization is always along the X-axis, and S-polarization along the Y-axis.

Light in a PBS is diverted in proportions dependent on the polarization of light. In ALT-COM, P-polarized light is transmitted straight through the interface, and S-polarized light is reflected at the interface perpendicularly [4]. The advantage to a PBS to another form of beam splitter is that light can be split in any proportion by controlling the polarization, which allows for combining a transmission and receive path. This ensuring that most of the received signal is used for accepting data rather than tracking.

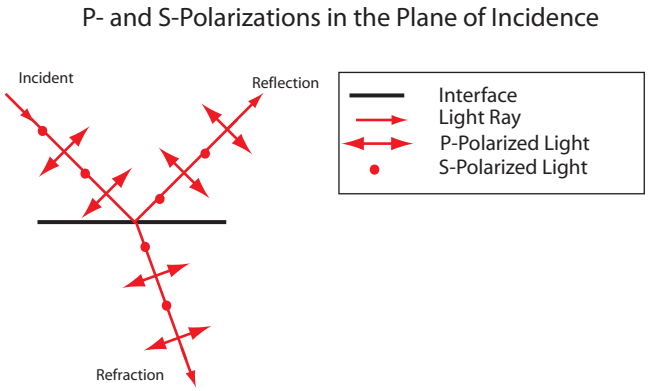

Figure 10. Plane of incidence at a dielectric boundary.

2.6.2 Quad-Cell Detector

A quad-cell detector can be used to detect small deviations in a laser signals position. When the communication link is created, the incoming signal is split (via a polarizer beam splitter) and part is directed to a tracking detector. When both stations are aligned properly, the beam is centered on four photovoltaic cells. Deviations of position can be tracked by comparing the voltages induced on each of the cells.

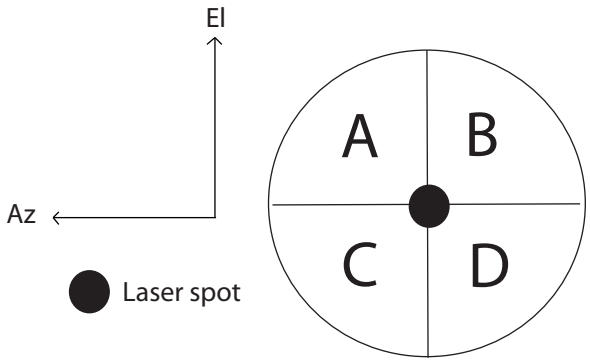

Figure 11. Quad-cell detector.

Figure 11 shows an example of a well-centered beam on a quad-cell and introduces labels to each cell. By designating the voltage on each cell, V_z, where z is that cells label, the deviation from centered can be expressed in voltage. Consider, in this example, that left-to-right deviations are due to errors in the azimuth angle (Az) and top-to-bottom deviations due to errors in the elevation angle (El). The angle deviations are related in volts as follows:

$$\text{Error in Az } = (V_A + V_C) - (V_B + V_D) \tag{1}$$

$$\text{Error in El } = (V_A + V_B) - (V_C + V_D) \tag{2}$$

As the voltages are proportionate to the amount of light each cell is receiving, the centering condition is to bring these errors to zero. These errors, after appropriate scaling, can be fed to the FSM to compensate. The scaling is necessary to account for describing the angular error in terms of voltage, and to match the transmitted error signal to the sensitivity of the FSM.

2.6.3 Shack-Hartmann Wavefront Sensor

In order to test the quality of the signal, a Shack-Hartmann wavefront sensor (WFS) was used at several points of development. The WFS is used to compare the beam profile to some standard profile, typically a plane wave incident flatly on the sensor. Analysis of the beam propagation used such a reference that was provided with the commercial sensor.

In order to test the phase, the beam is effectively sampled in multiple locations by being passed through an area of small lenslets. Each lenslet focuses part of the beam onto a focal plane array. The location is determined by the average phase across the lens. Creation of a reference profile tests the intensity on the pixels of the focal plane array in order to determine the Areas of Interest (AoI), which only contain light focused from a single lenslet. A final part of this calculation is to align the edges of the AoI evenly across the focal plane [11].

During analysis, the incident beam is split and focused into many of the AoI. The focal point of the beam is compared to the focal point of the AoI, in order to determine what the difference of the phase is for each area. With this information, the wavefront may be reconstructed through different algorithms – notably modal [11].

Modal reconstruction fits this data to Zernike polynomials. Zernike polynomials are particularly useful for circular apertures, as each term describes commonly observed beam aberrations such as: tip-tilt, focus, astigmatism, and many higher order aberrations. Because of this, each type of aberration can be qualitatively described with modal reconstruction. However, this method uses all AoI in computation. Since small beam sizes are used in ALT-COM, this reconstruction requires data masking (i.e. setting a definite boundary as to which AoI to consider) [11].

The WFS is sensitive and requires heavily attenuated beams (less than 1 μW) in order to provide accurate readings. Included software could calculate beam divergences in the far field. These calculations were augmented by a program created by Tim Williams which was known to be more accurate [3].

3. METHODOLOGY

Advanced Lasercom Systems and Operations Group at MIT Lincoln Laboratory has helped to establish feasibility of air-to-space lasercom systems. For the technology to be useful, it must be scaled down to a deployable size and weight. In meeting this goal, new hardware has been used and the performance of the hardware has been investigated. Furthermore, changes of hardware required interfacing between new and old components.

3.1 GOALS

The goal of this project was to design, build and test an Aircraft Lasercom Terminal Compact Optical Module (ALT-COM). The conceptual design for ALT-COM is shown in Figure 12.

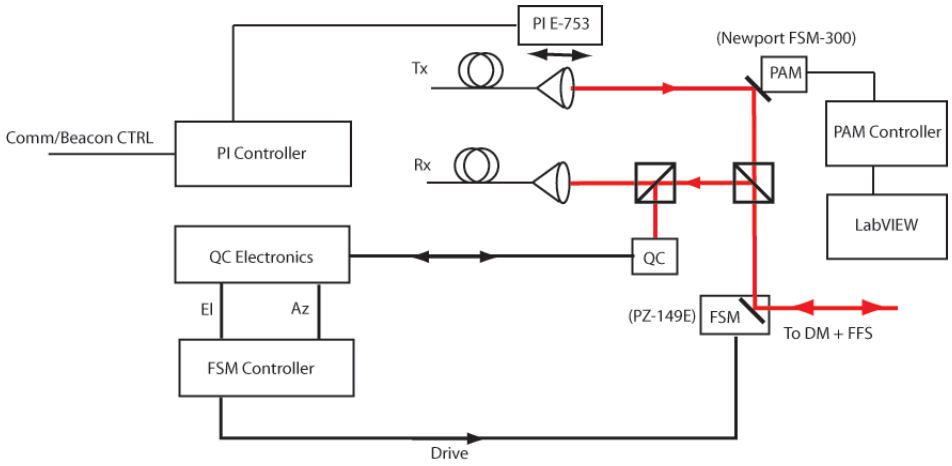

Figure 12. Aircraft Lasercom Terminal Compact Optical Module.

3.1.1 Decrease Size, Weight and Cost

The current Testbed setup includes two laser sources (a beacon and a communication signal) as well as two sensors (a focal plane array (FPA) and a quad-cell (QC)). Removal or replacement of these parts helped to lower the size and weight of the terminal.

The use of a lens on a mobile platform allowed a single laser FLA to operate in both the beacon and communication modes. Key characteristics examined are the switching speed between modes, and the beam divergence in these modes.

The FPA and the QC are used to acquire and track targets respectively. Removal of the FPA will did not require any additional components as the quad-cell will now be used to acquire targets.

In addition to the removal of components, mostly commercial-off-the-shelf (COTS) optics and devices have been used throughout the terminal. This reduces cost and availability problems with any components required.

3.1.2 Investigate New Hardware

Two new components have been introduced – a piezoelectric stage and a new fast-steering mirror. The piezoelectric stage replaces the functionality of the beacon Tx FLA. By moving a lens small distances (400 μm in ALT-COM) a single FLA is able to send both the beacon signal as well as handle data transmission. Operation of the stage and lens has been characterized by switching time between modes and beam divergence in the beacon mode.

A new platform has been used in place of the current FSM. A tip-tilt platform with a mirror mounted has been used rather than a traditional FSM. This was chosen for its more compact design. The range of operation and frequency responses have been noted.

3.1.3 Characterization of the Compact Terminal

As the individual components of ALT-COM were installed, optical alignment was performed. Mounts were adjusted in order to obtain proper alignment. Accordingly, performance was monitored in parallel to construction. This enabled verification of individual components as well as the ability to characterize the terminal. Operation parameters (i.e. mechanical performance) as well as signal integrity were documented throughout construction. There were six main objectives for the ALT-COM project. These objectives are listed below. For each objective there were certain parameters that needed to be satisfied for project success.

Objective 1: Working Tx FLA hardware and controller with beacon and communication beam switch controllability using PI PZT stage

1. Measure divergence of beacon and communication beams on wavefront sensor (WFS)
2. Demonstrate switching time <50 μsec for 400-um travel

Objective 2: Control of point-ahead mirror (PAM) for Tx FLA path

1. Control PAM to remain at fixed position within $\pm$10 μrad
2. Command PAM to perform spiral scan

Objective 3: Layout and optical alignment of ALT-COM components on approximately 12 x 18 in breadboard

1. Throughput loss $<$ 3 dB in Tx and Rx paths
2. Verify beam size to be roughly 4.4 mm diameter

Objective 4: Interface PI FSM to quad-cell (QC) controller for tracking feedback loop

1. Verify PI FSM receives tracking command from QC controller and feedback control loop functions

Objective 5: Complete evaluation of PI FSM for use as tracking mirror in conjunction with QC

1. Measure tracking PSD and residual jitter to be <20 μrads out to 1 kHz
2. Test mirror bandwidth
3. Test stroke of mirror in azimuth and elevation

Objective 6: Final Report and presentation

1. Deliver final report
2. Deliver final presentation on 10/15/2008

4. RESULTS

4.1 LAYOUT AND DESIGN

The conceptual design of ALT-COM has been based on Tim Williams' earlier work which introduced the piezoelectric stage as a switch between the beacon and communication modes. ALT-COM extends this work, introducing a more compact FSM and replacement of an FPA with a QC. The layout of ALT-COM was designed to fit onto an compact area of 12 × 18 in.

In designing mounting fixtures, it was necessary to consider the height of the optical axis. The PAM, being the most likely to be problematic to raise, was used to determine that 1.5 inches (37.5 mm) was the appropriate height for the optical axis. All components were noted to fall at or below this height before being placed on mounts.

Having decided on 37.5 mm for the height of the optical axis, it is imperative to ensure that the beam height remains at this level. By satisfying this requirement for the transmission beam, it is ensured for the receive beam as well. The reason for this is the common optical path used for communications; the incoming beam must travel backward along part of the transmission path, which satisfies this condition.

In order to test this, the beam is sent through a small iris mounted on the optical table. The iris is then bolted further back to check if the beam still passes through the iris. By using a transparent ruler, the error can be approximated. Possible error sources include the transmission fiber not being centered on the lens (only up-down deviations will affect the optical axis height) or an innate tilt in the Tx-FLA (due to an uneven tipping). Although the FLA tipping was a potential problem, it also allowed for fine tuning of the height of the fiber (note that this may also change the height of the optical axis).

In order to characterize the beam, a WFS was utilized. The sensor was mounted onto the work table, and required that ALT-COM be temporarily raised for testing purposes only. It could measure the wavefront and, through included software, calculate many additional parameters. Of interest, beam divergences, beam size, and Strehl ratio.

4.2 FINAL LAYOUT

During initial drafting, complete information of the quad-cell was not available, nor was a mount design available. Therefore, multiple options were initially developed. The final design, shown in Figure 13, was ultimately constrained by a large X-Y-Z stage used as the quad-cell mount for ease of beam alignment. During development, the different options were reviewed. With the addition of a new, smaller Rx FLA mount, it was possible to compensate for a large quad-cell mount. Figure 14 is a photograph of ALT-COM in its completed state; the quad-cell mount can be seen on the right side of the board.

The final design also eliminated the need of a waveplate between the two PBS cubes. A vast majority of light coming from the first PBS is already properly polarized to be reflected to the Rx

FLA, allowing much of the power to be using in data communication. The quad-cell was observed and tested to work without this waveplate in place, working from minor imperfections in the PBS transmissions and reflections. It is estimated that roughly 95% of the power into the second PBS travels the path to the receive fiber and about 5% appears at the quad-cell.

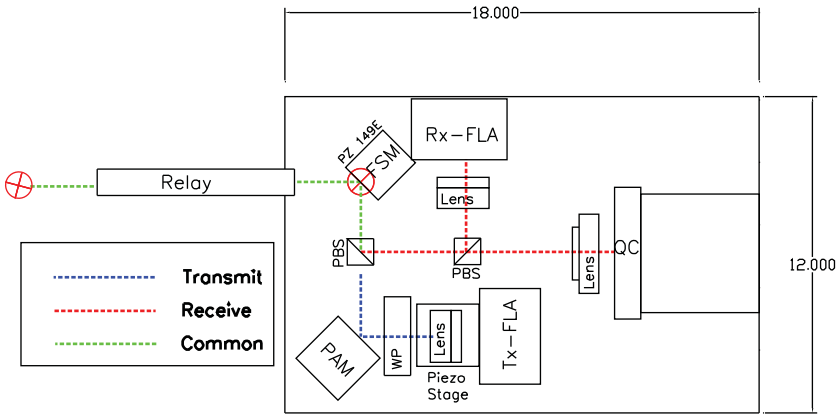

Figure 13. Final schematic for ALT-COM.

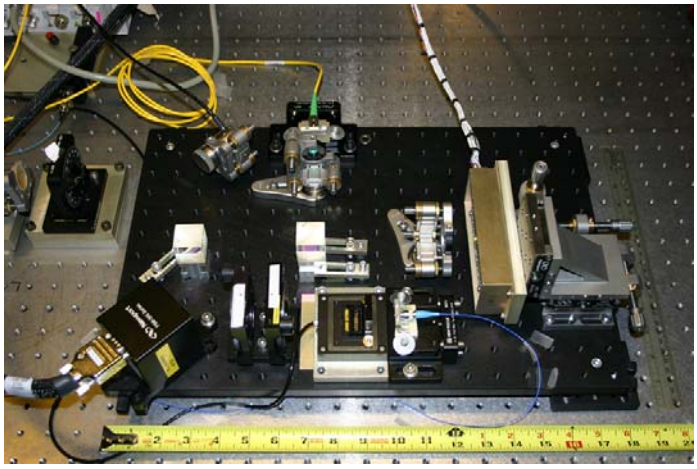

Figure 14. Photograph of completed ALT-COM.

4.3 MOUNT AND TEST TRANSMIT FIBER LAUNCH ASSEMBLY

The FLAs used in ALT-COM consist of a fiber clamp on X-Y tip-tilt stages. The stages eased initial alignments by providing a fine tuning mechanism. For the terminal transmitter, polarization maintaining (PM) fibers were used to maintain alignment of the output polarization state with the ALT-COM PBS cubes. These fiber optics help maintain the polarization of light more effectively

than standard fibers, though stress and strain on the fiber have noticeable effects on polarity. These are used due to the presence of polarizing components - notably the the beam splitters. Without control of polarization, there is unnecessary power loss from the first PBS.

PM fibers maintain polarization by creating two axes with different refractive indices. In 'PANDA' style fiber (used in ALT-COM) two stress rods are placed in the fiber do this. Linearly polarized light is transmitted along a single axis and remains on this axis throughout propagation. However, every fiber interface has potential issues in alignment, and must be checked to avoid problems. Use of a THORLABS polarimeter, Model No. PA530, helped identify poor interfacing due to an extraneous interface which was later bypassed.

In order to create a nearly planar beam from the Tx FLA, the optical fiber source must be placed at the focal point of the lens on the piezoelectric stage. Naturally, the stage is kept in the desired position for communications during this stage. Fine alignment is achieved with the mounting stage of the Tx FLA. For the beacon signal, however, the directional change of the lens must be considered.

If the stage is moved from the focal point, towards the fiber, the beam will only diverge. This situation was implemented for simplicity in avoiding the converging portion of the beam. Both cases are illustrated in Figure 15. Note that in the diverging case, an effective focus can be calculated before the lens. This effective focus is where the diverging rays seem to have once been focused and can be estimated with Equation 3. S_1 is the object to lens distance, S_2 is the position of the image (focus) which is positive behind the lens (and negative before it), and f is the focal length which is positive for converging lenses and negative for diverging lenses.

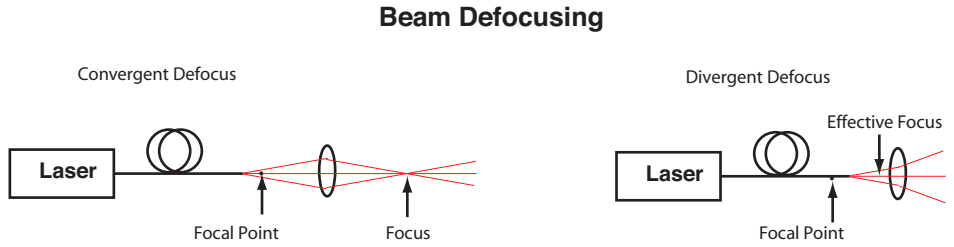

Figure 15. Examples of defocusing laser light from a fiber.

$$\frac{1}{S_1} + \frac{1}{S_2} = \frac{1}{f} \tag{3}$$

The Physik Instrumente stage, Model No. E-753, was controlled to move the lens to obtain both the beacon and communication beams. A program was written for the PC to interface with the PI E-753 controller through an RS-232 connection, in order to switch between modes.

4.3.1 Stage Control Software

The PI stage used in the beacon system has a range of 0 to 500 μm in closed-loop mode. At rest the PI Stage is at 0 μm. Since the PI Stage needs to be placed adjacent to the transmit fiber launch tip/tilt platform on the optical breadboard, the stage was mounted in the reverse direction in order to overcome obstruction of the control wire. Therefore, 0 μm is the distance of the lens for communication, and 400 μm the distance for the beacon beam.

In order to control the piezoelectric stage through the PI E-753 controller an interface was written for the PC. This program allows the user to switch between beacon and communication beam distances on the stage. The user can also type in the desired distances in μm for each mode.

The PC program was written in Microsoft Visual Basic .NET using the MSComm ActiveX control. Through this control the program sends serial commands through the COM port of the computer to the PI E-753 controller. The controller is configured with a General Command Syntax (GCS) in which parameters of the controller can be set and read.

When the program is opened, a window appears with four buttons and four text boxes (see Figure 16). The top button, upon being clicked, opens the PC serial port, and sends out two commands to the controller. When the port is opened the text box to the right notifies the user. The first command, when this button is clicked, sets the controller to closed loop mode. In this mode the controller monitors the position of the piezoelectric stage through an internal sensor and adjusts the position accordingly.

The next two text fields allow the user to input the desired distances for the length for both modes of communication. The user can invoke the position by pressing the corresponding button below the text field. At any time the port is open, the user can poll the current position of the stage by pressing the "Poll Position" button and read the value provided in the text box below.

4.3.2 Switching Speed

Switching speed of the piezoelectric stage was tested after installation of the Rx-FLA. The objective was to verify switching speeds remained under 50 milliseconds. A LeCroy WavePro 7100A oscilloscope was used to monitor the power on the receive fiber. The fiber was directly coupled to the input of the oscilloscope with an optical to electrical converter, and the waveform monitored.

The oscilloscope displayed a waveform of the power amplitude on the line. The stage control software was used to switch between beacon and communication modes. By switching between modes, the power amplitude switches between two levels. Since the communication beam has less divergence, more power appears at the fiber-coupled receiver. The communication beam is the higher power level. Therefore the fall-time represents the amount of time to switch from communication to beacon mode. The rise-time is the amount of time to switch from beacon to communication mode.

The oscilloscope has a built-in feature to detect rise and fall times and compute these values. It computes these times based on the amount of time to change from 10% to 90% of the final amplitude value. The oscilloscope display is shown in Figure 17. The top display shows the power

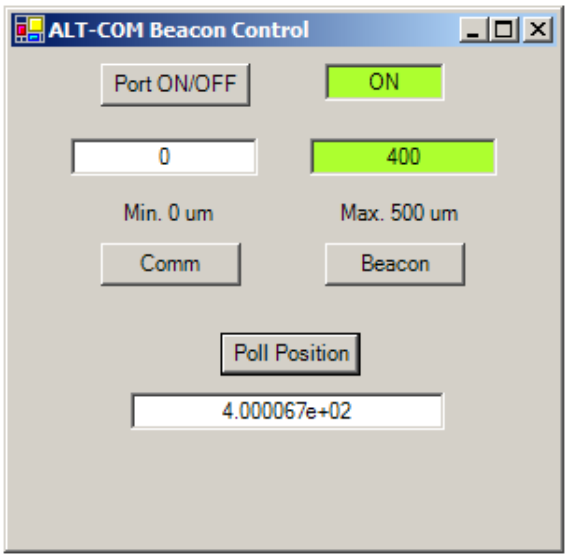

Figure 16. Beacon control software GUI.

trace, where both rise and fall transitions occur. Oscillations are visible in the communication mode due to power fluctuations later diminished (see Section 4.5). The bottom trace displays a zoomed-in version of the beacon to communication mode transition.

Ten trials were conducted, with each trial including both transitions. The beacon to communication and communication to beacon switching speeds are displayed in Table 1.

The average switching speed from beacon to communication mode for the ten conducted trials was 8.70 $\pm$ 1.03 msec standard deviation. The communication to beacon switching speed was measured to be 9.37 $\pm$ 0.77 msec. These values confirm that the piezoelectric stage is capable of switching modes under 50 msec.

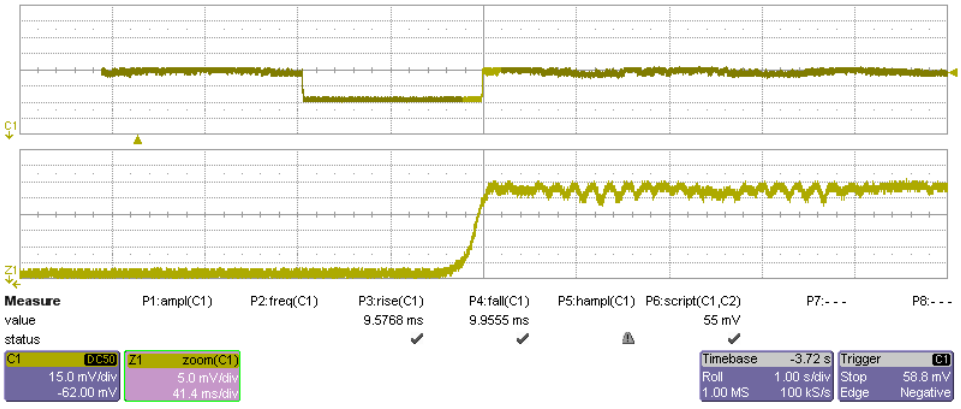

Figure 17. Switching speed: transition time between Rx power levels.

TABLE 1

Switching Speed Measurements

Trial	Beacon to Comm Speed (msec)	Comm to Beacon Speed (msec)
1	8.246	8.893
2	8.456	9.948
3	10.030	10.115
4	7.527	7.947
5	8.216	10.126
6	8.296	8.954
7	7.883	8.542
8	10.707	10.007
9	8.076	9.230
10	9.577	9.956
Mean	8.701	9.372
Std. Dev.	1.036	0.770

4.3.3 Beam Leveling

Beam leveling was facilitated by the use of an iris. This iris was mounted on a block in order achieve a height close to that of the beam from the Tx FLA. It was first placed on the outside edge of the optical breadboard. The aperture size was minimized (to 1.5 mm) and then the height was verified by checking passage of the beam through the iris. The iris was then moved farther away from the breadboard and beam passage was checked again. When the beam did not pass through the iris at both locations, the tip/tilt platform for the Tx FLA was adjusted, and the beam height was again tested.

4.3.4 Beam Characterization

The wavefront sensor first needed to be relocated from near the Tracking Testbed to the work area for ALT-COM. The sensor was then leveled with the beam from ALT-COM.

Use of the sensor at each testing stage required reposition and alignment. A mirror was mounted in front of the lens. An aperture surrounded by infrared paper was used to perform coarse alignment. First, the aperture was placed in front of the mirror, which was adjusted until the beam was directed near to the aperture. Similarly near the source, the beam passed through the aperture and its reflection was directed back onto the aperture. Fine alignment with the tip-tilt stage was possible at this point using software to calculate and display the average beam tilt.

Once the mirror was removed, the sensor was ready for operation. The detectors are highly sensitive and prone to saturate with laser sources. If not accounted for, the sensor would have been unable to recognize differences in power above saturation level. For this reason, the power was attenuated to less than $1\mu W$. An Oz-Optics variable optical attenuator (VOA), Model No.

DA-100-35-1550, was used to compensate for the sensitivity. Saturation levels of about 80% are best, although any higher values (below full saturation) are comparable.

Figure 18 and Figure 19 show a reconstructed wavefront after the Tx FLA, for the comm and beacon beams respectively. The color grading measures from 0 to the maximum phase difference, refered to as the peak-to-valley (P-V) error. From this, a sense of how curved a wavefront is. The comm beam, for example, is largely colored in the red-yellow regime, signifying an approximately planar wavefront. Conversely, the color gradient of the beacon beam signifies a curve wavefront.

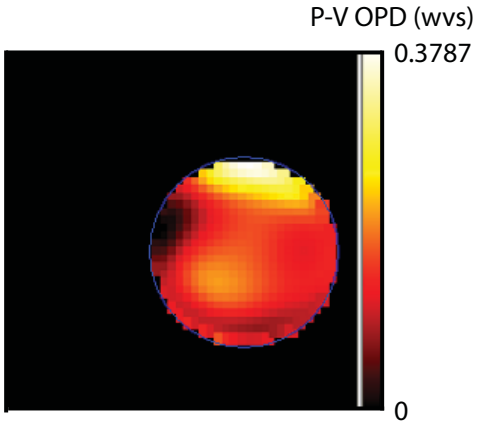

Figure 18. Phase-front of the communication beam after Tx FLA.

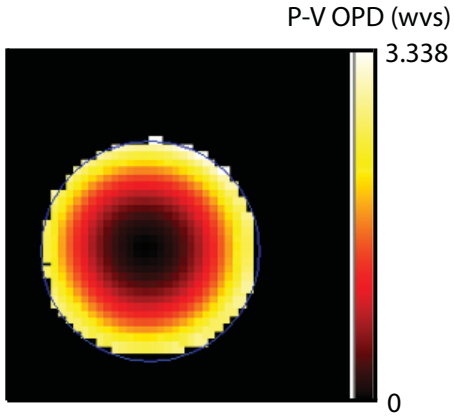

Figure 19. Phase-front of the beacon beam after Tx FLA.

With data from the wavefront sensor, wavefront error is known and used to calculate various other beam parameters, including beam width and beam divergence [11]. For the beam divergence, these calculations were augmented by a program created by Tim Williams which was known to be more accurate [3].

TABLE 2

Communication Beam Divergence $1/e^2$

	Components	X div $1/e^2$(mrad)	Y div $1/e^2$ (mrad)	Avg div $1/e^2$ (mrad)
Tx	Piezo Stage	0.566	0.590	0.578
	WP1	0.565	0.582	0.574
	PAM	0.564	0.582	0.573
	FSM	0.568	0.589	0.579
Rx	PBS1	0.570	0.588	0.579
	QWP (retro beam)	0.566	0.585	0.576
	PBS1 (retro beam)	0.563	0.578	0.571
	PBS2 (to Rx FLA)	0.576	0.589	0.583
	PBS2 (to QC)	0.567	0.591	0.579

TABLE 3

Beacon Beam Divergence $1/e^2$

	Components	X div $1/e^2$ (mrad)	Y div $1/e^2$ (mrad)	Avg div $1/e^2$ (mrad)
Tx	Piezo Stage	2.915	2.808	2.862
	WP1	2.736	2.724	2.730
	PAM	3.036	2.887	2.962
	PBS1	2.928	2.758	2.843
	FSM	3.141	2.892	3.017
Rx	QWP (retro beam)	3.096	2.854	2.975
	PBS1 (retro beam)	2.878	2.796	2.837
	PBS2 (to Rx FLA)	2.817	2.753	2.785
	PBS2 (to QC)	2.905	2.439	2.672

The beam of ALT-COM is elliptical due to alignment imperfections from the Tx FLA. The beam size is given as an average of the full width of the major and minor axis. For communication, this is 3.8 mm and 5.4 mm for beacon, both at a $1/e^2$ cut-off. These measurements are taken after the FSM, the final component in the transmission path.

Similarly to the beam size, the divergence is calculated as the average of the divergence along the major and minor axis. Divergences are shown throughout ALT-COM in Table 2 for communication and Table 3 for beacon. Note that components listed after the FSM are part of the receive path, and the beam was reflected from a mirror to obtain these measuremnents. From ALT-COM, the divergence for the communication beam is 0.58 mrad and 3.02 mrad for the beacon beam.

The WFS was also used to measure the wavefront error. These errors are due to imperfections in alignment, focusing, as well as manufacturing. The error is a measure of deviation in the phase of

TABLE 4

RMS Wavefront Error

Components	Communication RMS error (wv)	Beacon RMS Error(wv)
Piezo Stage	0.029	0.459
WP1	0.026	0.453
PAM	0.026	0.527
PBS1	0.027	0.517
QWP (retro beam)	0.026	0.524
PBS1 (retro beam)	0.028	0.626
PBS2 (retro beam)	0.028	0.590
PBS2 (to QC)	0.026	0.720

*Waves (***wv***) defined at* $\lambda = 1.55\ \mu m$.

light from a perfectly collimated beam– which has a flat wavefront. This can be expressed with the P-V wavefront aberration. However, it is generally more meaningful to state the root-mean-square (rms) wavefront error, which also takes into account the distribution of the error [13]. Measurement of the wavefront error is used throughout ALT-COM in order to ensure quality of the wavefront. A well-corrected wavefront will have a high Strehl Ratio, which is a measure of how well the beam can be focused for reception [10] [13]. The Maréchal criterion is used to qualify a beam as well-corrected. This criterion states a Strehl ratio of 0.8 or higher is considered well corrected; this corresponds to an rms $\leq \frac{\lambda}{14}$, or ≤ 0.0714 waves.

4.3.5 Power Measurements

In order for the communication systems to be effective, enough power must be transmitted for the signal to be identified. To establish a connection, this is particularly important as the beam energy is spread out across a larger area; this results in a lower intensity, which requires a larger receiver to detect. The amount of power necessary for detectors to measure a signal is referred to as its sensitivity, or noise floor. This is further limited since light from other sources may also be received as noise. The transmission beam must be considerably stronger than this light noise for appropriate acquisition.

The energy transmitted is not necessarily the same that is given by the laser source. As the laser passes through each component, some power is lost in absorption, imperfect transmission/reflection of surfaces, or scattering. Therefore, the losses were tracked during the construction of ALT-COM using two different meters; one which takes input from a fiber optic wire, and the other to detect the power of a beam in free space.

Testing power from a fiber optic required a power sensor module that could be connected to the laser chassis. The Agilent power sensor module, Model No. 81635A, has a standard female fiber connecter for input, and could be set to measure a variety of wavelengths. The output power into ALT-COM was measured after each junction to the transmission FLA, which was characterized in

the same manner before the fiber was mounted. These measurements were done in dBm – relative to the power of a one milli-watt (mW) laser (0 dBm). With a source power of 3.5 dBm, 1.37 dbM was transmitted from the Tx FLA. In order to measure the insertion loss to the Rx FLA, a test fiber was mounted both to test alignment and measure power using this method, but this measurement was done in dB, as with the free space components.

A free space power detector was used for the remaining components. The HP free space optical head, Model No. 81525A, connects to the HP module, Model No. 81533B, on the laser source chassis, which operates in a similar manner. Measurements were taken relative to the power coming out of the Tx FLA in dB. In order to best contain the beam, it was transmitted through a converging lens before being measured. No fixed mounts were available for the detector head, which was instead elevated on aluminum blocks for a consistent height relative to the converging lens.

Each optical component is undoubtedly exerting some amount of unwanted reflection/transmission, absorption, or an insertion loss (the Rx-FLA). Fortunately, these losses tend to occur as percentage losses, and do not need to be qualified by the absolute beam strength. In this way, the power cost of sending or receiving a signal is explored. In determining the laser output for a final system, power will need to be specified not only to the detectors needs, but also by the losses of sending and receiving the signal.

With each component's loss measured individually, the loss of ALT-COM as a whole is characterized. Losses are treated in individual cases, not requiring the same beam strength through each component. However, the beam was maintained for testing before and after the placement of each component.

The transmit path and receive path are treated as separate pieces for a few reasons. Many components exist on a single path, and will not be dependent on each other, allowing for separate consideration of either side. Furthermore, it helps to avoid confusion of double counting components that exist on the common beam path (the first PBS and the FSM). This could be especially critical if the PBS exhibited different efficiencies for reflection and transmission. However, although this was expected, both were observed to have a loss of 0.22 dB in the application of ALT-COM. Therefore, this value is used for losses described due to a PBS in general.

Table 5 lists the losses along the transmission path and Table 6 lists those along the receive path. The total losses are calculated as a sum as these losses act systematically. The goals for ALT-COM were to keep these losses below 3 dB, which was satisfied only for the transmission path (total loss of 0.62 dB). The receive path experiences most of its loss (total loss of 4.3 dB) due to insertion loss in the fiber (see Sec 4.5). This loss is due to difficulties associated with alignment for the laser-to-fiber coupling, and can be expected to improve with only minor design changes.

The power losses for ALT-COM were used in calculating a link budget for a communication link between an aircraft and spacecraft. This budget is used to identify all of the losses due to the transmitter, receiver, and the environment of the communication channel. This sort of budget can be used to characterize the losses throughout the entire links. Furthermore, the equations used to calculate losses can be used to explore how changing parameters effects the links overall [6]. The

TABLE 5

Power Loss along Transmission Path

Components	Loss Measured (dB)
Waveplates	0.06
PAM	0.14
PBS1	0.22
FSM	0.20
Sum	0.62

TABLE 6

Power Loss along Receive Path

Components	Loss Measured (dB)
FSM	0.20
PBS1	0.22
PBS2	0.22
Rx-FLA Insertion	3.7
Sum	4.3

power requirement of the receiver is given based on the data rate, R_D, and is dependent on the coding type which is implemented [1].

Table 7 shows the link budget for a link from a satellite to high-altitude aircraft where complex environmental effects are ignored. The satellite values are a conceptual model, whereas the aircraft values are based from ALT-COM's test results. This calculation predicts a that a 40 dBm (10 W) laser will be able to illuminate a sample satellite terminal with a total power of -44.49 dBm. This was further found to be sufficient to support a 2.5 Gb/s link. Note that this leaves a fairly small excess link margin of 0.53 dB.

Table 8 shows a similar link budget in the opposite direction– aircraft to satellite. The losses experienced in ALT-COM's receive path do not play a roll in this case, and therefore a power of -39.77 dBm can be delivered even with a similarly powered source. In this case, for a 2.5 Gb/s link, there is a larger link margin of 5.25 dB.

4.4 PAM AND FSM INPUT RESPONSE

In ALT-COM the azimuth and elevation of the PAM needed to be controlled through two analog inputs. These analog inputs were to be controlled by a National Instruments real-time PXI controller. During testing the FSM was to be controlled in open-loop command, through the analog inputs, in order to obtain proper beam alignment. For the final system, the FSM was controlled by feedback from the quad-cell. Although the mirrors were being commanded in open-loop, the

TABLE 7

Link Budget for Satellite to Aircraft

Parameter	Symbol	Value	Notes
Source Parameters and Geometry			
Wavelength	λ	1.55 μm	
Data Rate	R_D	2.5 Gb/s	
Range	R_S	40,000 km	Aircraft to GEO
Satellite Aperture Diameter	D_S	22.86 cm	9.0 in
Aircraft Aperture Diameter	D_A	3.81 cm	1.5 in
Link Budget			
Transmitted Power	P_T	+40.00 dBm	10 W
Satellite Tx Losses	L_{STx}	-5.00 dB	Notional value
Satellite Antenna Gain	G_S	+113.32	$= 20 * \log_{10}(\pi * D_S * 0.01/(\lambda * 0.000001)$
Path Loss	L_S	-290.22	$= 20 * \log_{10}(\lambda * 0.000001/(4 * \pi * R_S * 1000))$
Aircraft Antenna Gain	G_A	+97.75	$= 20 * \log_{10}(\pi * D_A * 0.01/(\lambda * 0.000001))$
Aircraft Rx Losses	L_{ARx}	-4.34	
FEC Coding Gain [1]	G_C	+4.00	
Total Receiver Power	P_r	-44.55 dBm	$= P_T + L_{STx} + G_S + L_S + G_A + L_{ARx} + G_C$
Margin			
Receiver Sensitivity	P_{req}	-45.02 dBm	$= -39 + 10 * \log_{10}(R_D/10)$
(EDFA pre-amp PPM)		50 phot/bit	Encoding Type
MARGIN		+0.53 dB	$= P_r - P_{req}$

TABLE 8

Link Budget for Aircraft to Satellite

Parameter	Symbol	Value	Notes
Source Parameters			
Wavelength	λ	1.55 μm	
Data Rate	R_D	2.5 Gb/s	
Range	R_S	40,000 km	Aircraft to GEO
Satellite Aperture Diameter	D_S	22.86 cm	9.0 in
Aircraft Aperture Diameter	D_A	3.81 cm	1.5 in
Link Budget			
Transmitted Power	P_T	+40.00 dBm	10 W
Aircraft Tx Losses	L_{ATx}	-0.62 dB	
Aircraft Antenna Gain	G_A	+97.75 dB	$= 20 * \log_{10}(\pi * D_A * 0.01/(\lambda * 0.000001))$
Path Loss	L_S	-290.22 dB	$= 20 * \log_{10}(\lambda * 0.000001/(4 * \pi * R_S * 1000))$
Satellite Antenna Gain	G_S	+113.32 dB	$= 20 * \log_{10}(\pi * D_S * 0.01/\lambda * 0.000001))$
Satellite Rx Losses	L_{SRx}	-5.00 dB	Notional
FEC Coding Gain [1]	G_C	+4.00 dB	
Total Receiver Power	P_r	-42.13 dBm	$= P_T + L_{ATx} + G_A + L_S + G_S + L_{SRx} + G_C$
Margin			
Receiver Sensitivity	P_{req}	-45.02 dBm	$= -39 + 10 * \log_{10}(R_D/10)$
(EDFA pre-amp PPM)		50 phot/bit	Encoding Type
MARGIN		+5.25 dB	$= P_{act} - P_{req}$

mirrors themselves have internal sensors that provide feedback in a control loop. Internal feedback can be turned on or off based on the application. We first tested the mirrors for angular response to voltage command. For this first test, internal feedback was enabled.

4.4.1 Voltage Response

In order to properly command both the PAM and FSM these components were first characterized to understand their response to external input. These components were controlled by analog signals from a National Instruments DAQ (Data Acquisition Hardware). The DAQ was commanded through test software in LabVIEW, which stepped through a range of voltages. A Newport autocollimator, Model No. LDS1000, was used to measure the angular response of the mirror. The autocollimator projects an image on the mirror and measures the deflection of the beam on its internal detector. Along with each voltage applied to the mirror's controller, the LabVIEW software also recorded the corresponding angle on the X and Y axes, more commonly known as the azimuth and elevation axes respectively. The output signal of the autocollimator was monitored through a GPIB connection. The test setup is shown in Figure 20.

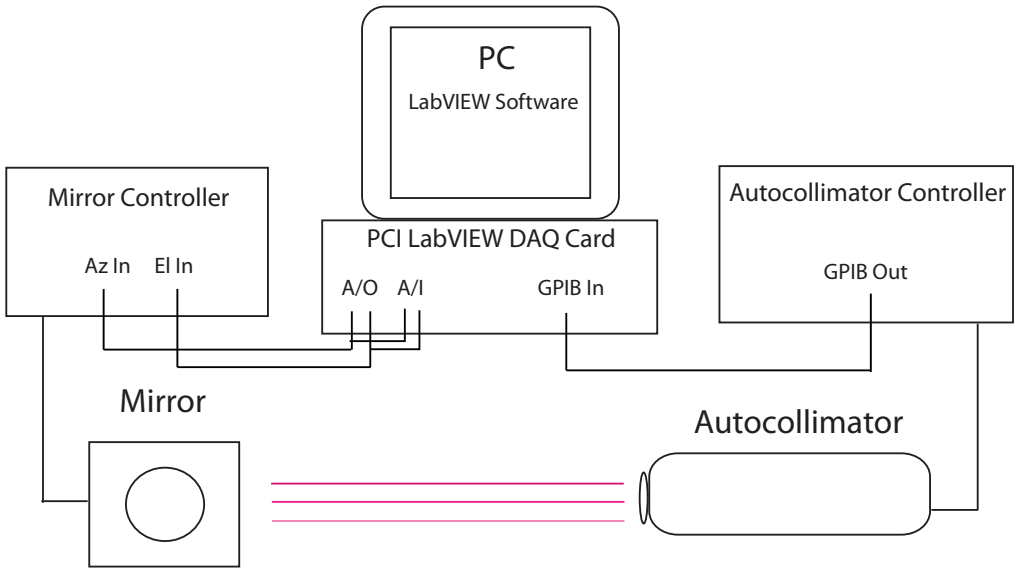

Figure 20. Voltage response test setup.

Since the controller of each mirror had two inputs for each axes, the axes were tested with the routine independently. The Az axis was commanded with the range of voltages, and then the El axis was commanded. The LabVIEW test software created a Microsoft Excel sheet with the voltage for each axis along with the corresponding angle. The data was then plotted and viewed in order to verify the linearity between voltage and mirror angle. A linear regression was computed for the data and then the slopes were recorded and later used in the development of software for the PAM.

The PAM has an input range of -10 V to 10 V. This corresponds to ±26.2 mrad angular movement of the shaft. The resulting angle after beam reflection is double the mechanical angle of the shaft. The PAM was tested with a range from -1 V to 1 V with a step size of 0.1 V. This voltage range was selected to move the mirror approximately ±2620 μrad. This enabled us to collect data over the full range of the autocollimator from ±2000 μrad. The ALT-COM FSM, PI S-330, has an available range of -1 V to 12 V. This covers a nominal range of 2 mrad in closed loop operation. The FSM was tested with a range from -1 V to 10 V as the NI DAQ device is limited to an output of 10 V.

The voltage response for the FSM will first be discussed. The FSM was tested with internal feedback enabled and disabled in order see the difference in dynamic range. With 0 V applied to both axes the autocollimator displayed an Az angle of 8 μrad and an El angle of 56 μrad. This was the human error in calibrating the autocollimator. The voltage response test was conducted for the mirror and then these values were subtracted from the recorded angles. The FSM voltage response with internal feedback enabled is shown in Figure 21. After completing linear regression on the samples in MATLAB, the y-intercepts and slopes were recorded for each input. The y-intercept for the Az axis is at 0.13 μrad while the El axis crosses at -13.43 μrad. The slopes for each axis differed by about 14 μrad. The slope for Az is -179.98 μrad/V while the slope for El is -193.01 μrad/V.

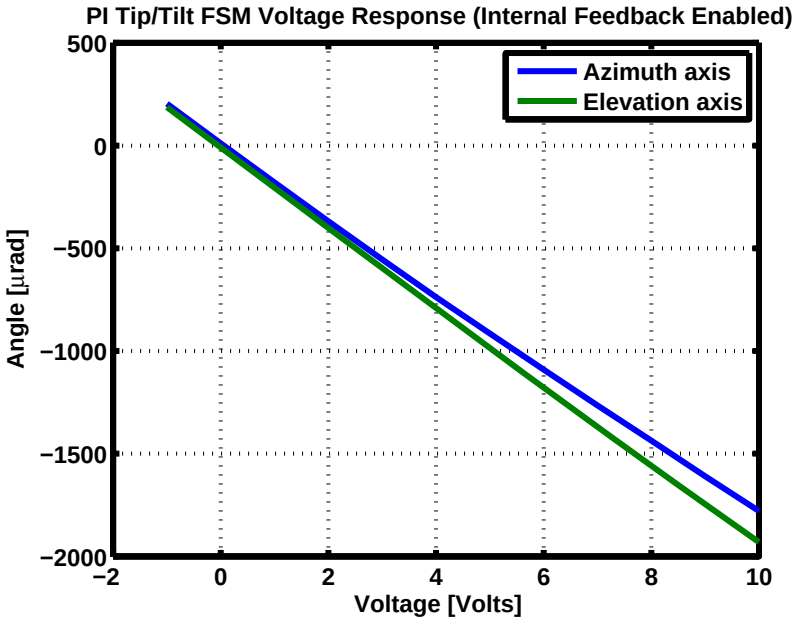

Figure 21. FSM voltage response (internal feedback enabled).

With internal feedback disabled the responses are not as linear. The most linear region, displayed in Figure 22, is over the range 0 to 8 V. Linear regression was computed to show that Az and El share an offset of around 170 μrad with 0 V applied. Although not completely representative

of the curves, the slope for Az is -224.55 μrad/V and the slope for El is -245.34 μrad/V. The inputs are more responsive to an input voltage with internal feedback disabled than enabled.

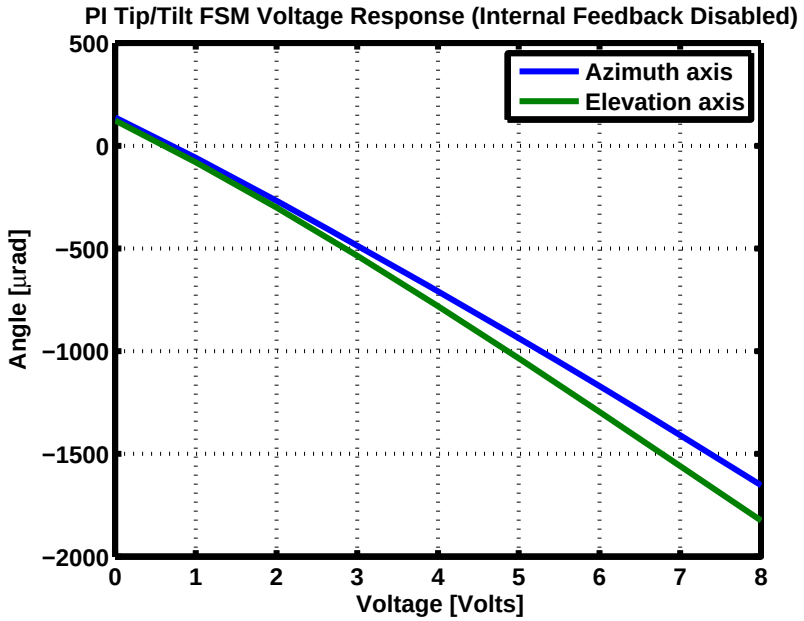

Figure 22. FSM voltage response (internal feedback disabled).

The PAM voltage response was tested with internal feedback enabled only, as internal feedback was to be used with open-loop command of the mirror. The voltage response of the Newport FSM-300 mirror is shown in Figure 23. With 0 V applied to each input the mirror is close to the null position. The slope for Az is 2910.7 μrad/V and the slope for El is -2777.3 μrad/V.

4.4.2 PAM Control Software

The point-ahead mirror serves the purpose of directing the beam ahead of the spacecraft terminal. The mirror also plays an important role in acquisition of the air-to-space link. While the laser beam is in beacon mode, the point-ahead mirror moves in a spiral fashion in order to scan a wider range for the spacecraft.

The Newport FSM-300 mirror provides ±26.2 milliradians of mechanical angular range by controlling two axes. The controller for the PAM has two analog inputs (X and Y) for external control of the mirror, the inputs can range from ±10 V. The PAM controller in the TTB is currently commanded by a National Instruments PXI box running NI LabVIEW 8.2.1 real-time software. The PXI box is controlled by a PC through a remote connection.

The graphical software on the remote PC, currently running in the TTB, that controls the Newport mirror implements the spiral scan task and the state machine of the terminal. The same software has been modified for use in the ALT-COM PAM. The spiral scan task was removed from

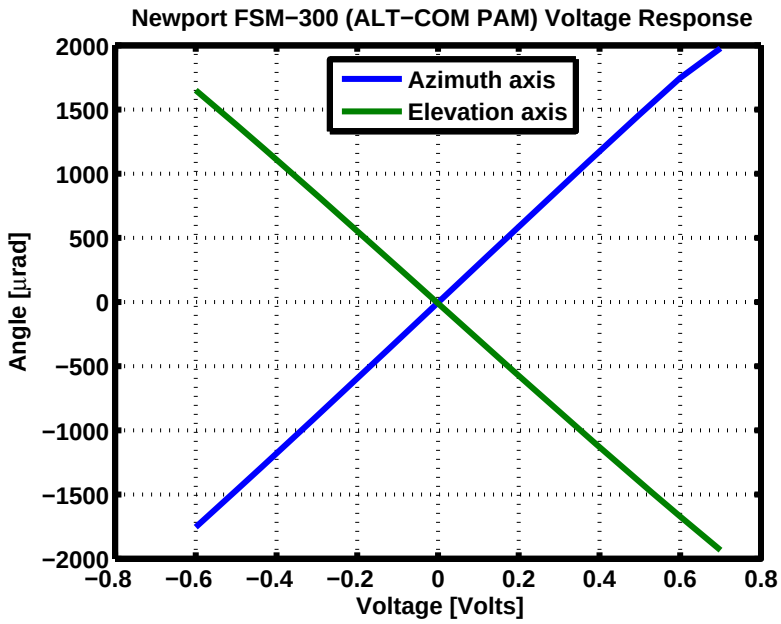

Figure 23. Newport FSM-300 voltage response.

the terminal software and additional features were added. User inputs were added to the existing software such that the user can command the mirror's position. This modified software was later tested to insure that the software can control within ±10 μrad. The autocollimator, that used earlier to characterize the PAM, was utilized to verify this level of control.

The required maximum angle for the spiral scan is 2 milliradians. The parameters found during characterization of the PAM were used to scale the Az and El inputs to obtain the required range. Additionally the commands were altered to account for the 45° angle of the beam incident on the PAM.

LabVIEW software was written to command the PAM in open-loop. This software allows the user to input a value for both Az and El in microradians. This software was written using the response slopes from mirror characterization. The graphical programming of the PAM open-loop command software is shown in Figure 24.

The requirement for this software was to obtain control of the PAM within ±10 μrad of a commanded position. This was tested by first commanding the PAM with 0 V on each input. The corresponding offset angles were recorded from the display of the autocollimator.

The software was then used to command the PAM to various positions. The angle for each axis was recorded and the offset was subtracted from the value. The offset was 29.5 μrad/v for Az and -46.5 μrad/V for El. The response angle was then compared to the commanded angle, and the amount of precision was recorded. The response slopes were then adjusted accordingly in the software. The final response slopes were 2930.7 μrad/V for Az and -2777.7 μrad/V for El. The average precision for Az was -6.79 μrad and 10.13 μrad for El. Radial precision found for each

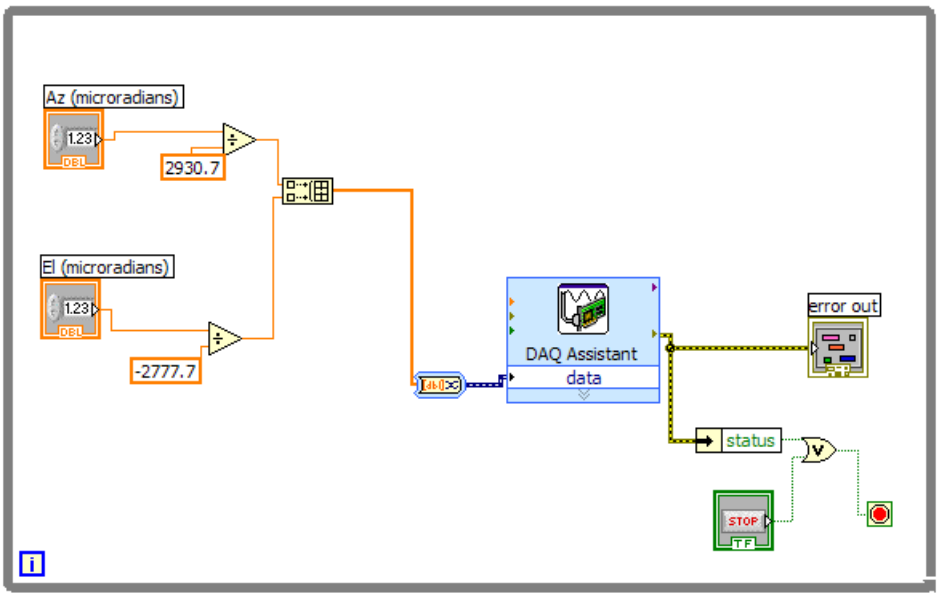

Figure 24. PAM open-loop command software in LabVIEW.

command by computing the length of the 2-D vector. The average radial precision was 13.40 μrad. The fact that most of the angular responses for Az were negative and El were positive suggests that there is an offset to the PAM. This offset was not found during the voltage response tests as the autocollimator was calibrated to the null position of the PAM. This test removed offset during the adjusted response, assuming the offset was calibration error with the autocollimator, however some of the offset must be due to the PAM. Table 9 displays the commanded angles and adjusted response angles.

In addition to manual positioning of the PAM, a spiral scan routine was developed from existing LabVIEW software. The spiral scan routine is used by the aircraft during acquisition and tracking to locate and maintain the link with the spacecraft. The existing LabVIEW software used in the TTB was modified by replacing the scale factors used for both the azimuth and elevation axes. The region covered by the spiral scan routine was modified to be approximately ± 2 mrad for each axis.

The highest level function of the spiral scan routine is called the scan player. The function is shown in Figure 25. This function first reads in two data files within the function 'READ CLV SPIRAL'. These contain the voltage values to command both the azimuth and elevation axes over time. The rate at which these values are written to the DAQ (clock rate) is chosen by the user in the GUI.

The function 'READ CLV SPIRAL' was modified for the ALT-COM spiral scan routine. The function is shown in Figure 27. One-hundred samples of the voltage data files provide a spiral scan with radius 0.01 V. This approximately corresponds to a ± 0.262 mrad region for each axis (± 26.2 mrad for ± 10 V input range). Therefore each sample was multiplied by 1000 for the desired range.

TABLE 9

PAM Command Response

Command (μrad)		Adjusted Response(μrad)				
Az	**El**	**Az**	**Precision**	**El**	**Precision**	**Radial Precision**
200	200	197	-3	202.3	2.3	3.780
300	300	296	-4	302.7	2.7	4.826
400	400	394.9	-5.1	406.8	6.8	8.500
500	500	494.9	-5.1	507.9	7.9	9.403
700	700	694.8	-5.2	711.9	11.9	12.987
1000	1000	992.8	-7.2	1014.8	14.8	16.458
1200	1200	1190.7	-9.3	1222	22	23.885
1400	1400	1387	-13	1421	21	24.698
400	800	388.9	-11.1	808.6	8.6	14.042
800	400	799.4	-0.6	409.8	9.8	9.818
100	1200	78.5	-21.5	1203.8	3.8	21.833
1200	100	1203.6	3.6	110	10	10.628

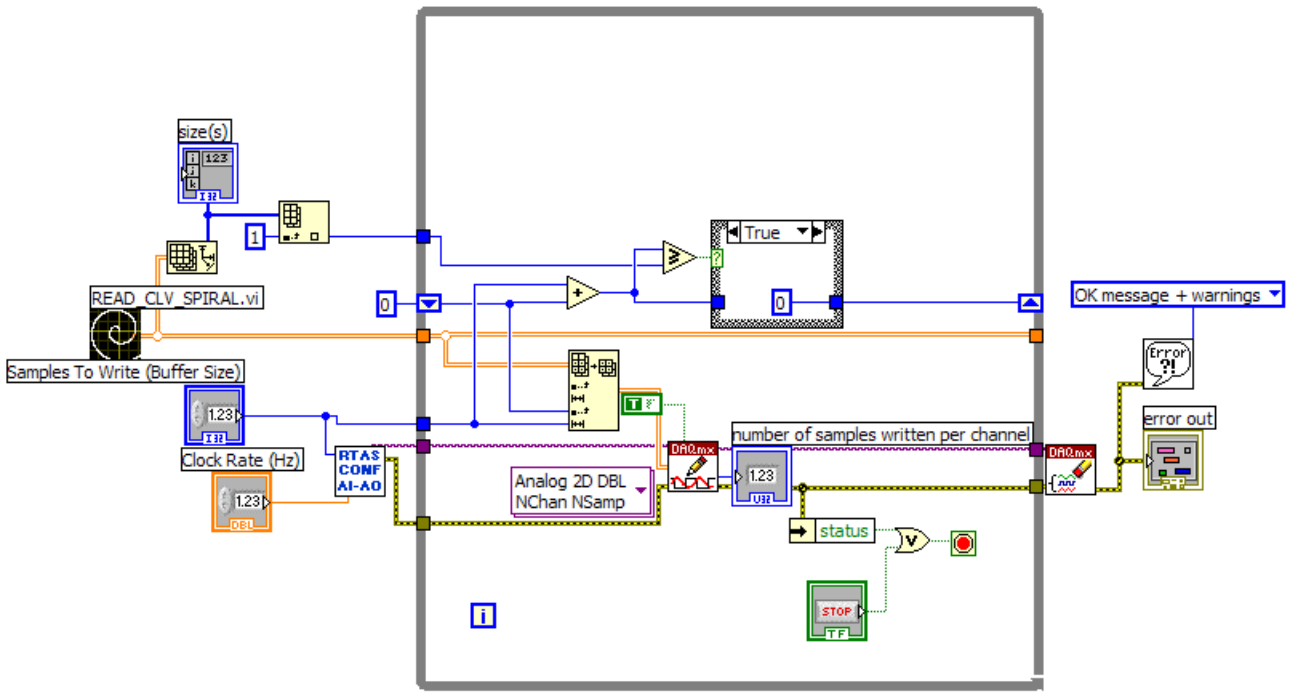

Figure 25. PAM spiral scan player in LabVIEW.

Additionally the azimuth input was scaled by 2903.7/2777.7 to account for the different slopes of each axis found during the voltage response tests.

The elevation angle needed an additional correction for physical reasons. The angular outputs given by the 'READ CLV SPIRAL' function were the desired response of the mirror, however the initial tilt of the mirror affected this response. Figure 26 demonstrates how small angle changes in elevation reflect the beam at small angles than expected by the mechanical tilt. This is due to the rotational axis for elevation no longer being orthogonal which results in a trigonometric scaling of the angular change. For this reason, the elevation angles are divided by that scale, cos(45), in Figure 27.

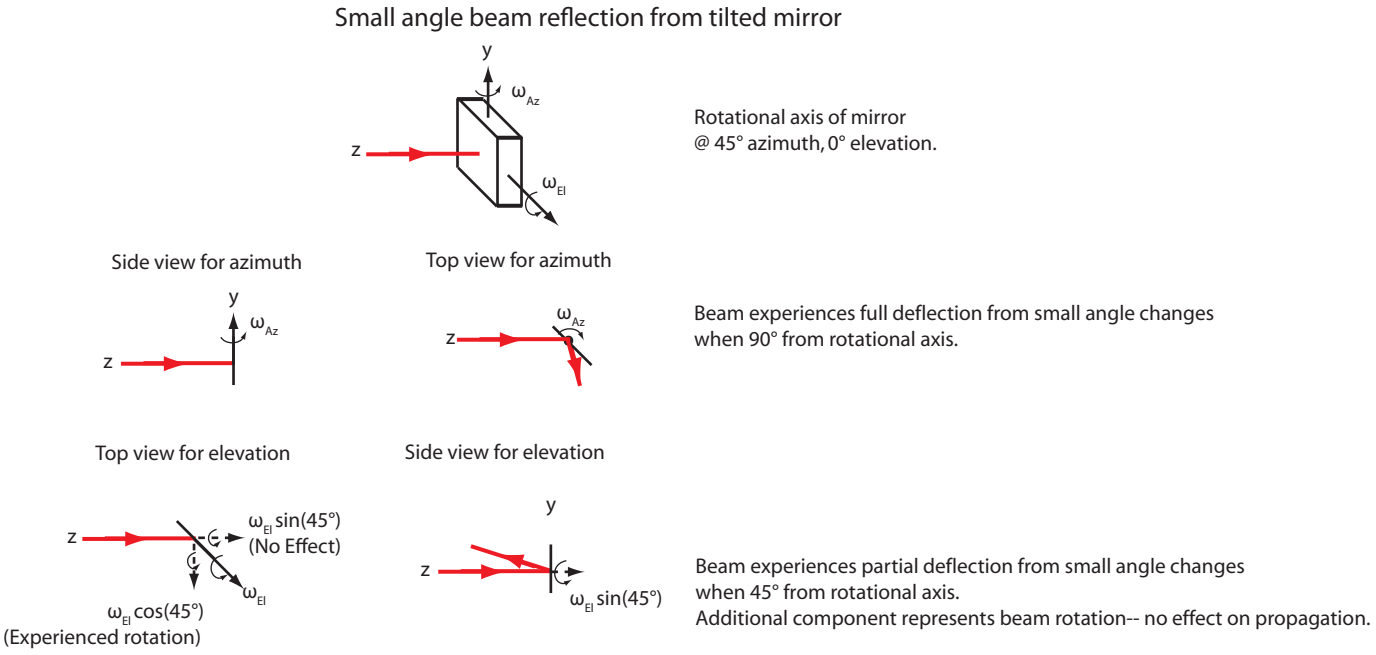

Figure 26. Reflection from a tilted mirror.

By changing parameters in the software we were able to obtain roughly ±2 mrad range for spiral scan. This range is the mechanical movement of the mirror shaft. The beam is seen to deflect at a half angle determined by the mirror's change in angle. This is because the mirror's mechanical tilt changes the angle between the beam and the surface normal. As the beam must deflect this extra distance from the normal, it will experience a deflection twice that of the mirror's tilt as shown in Figure 28.

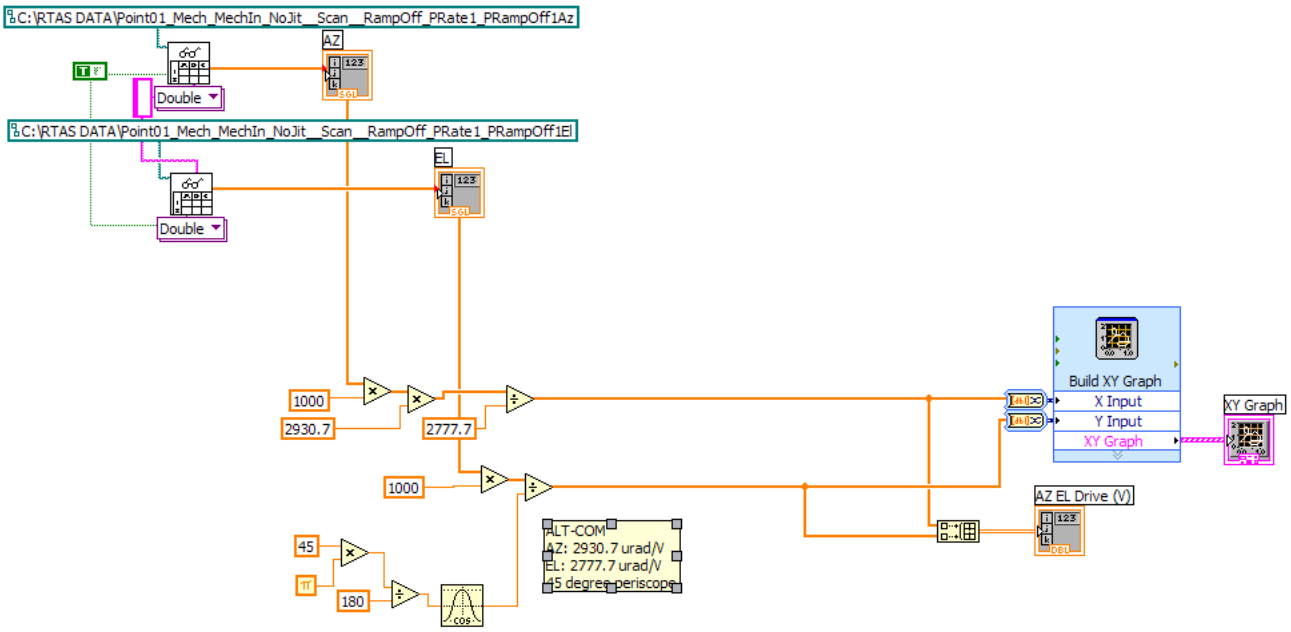

Figure 27. PAM spiral scan reader in LabVIEW.

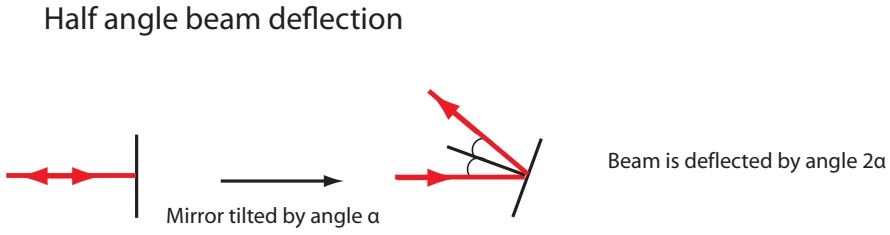

Figure 28. Half-angle reflection from tilting a mirror.

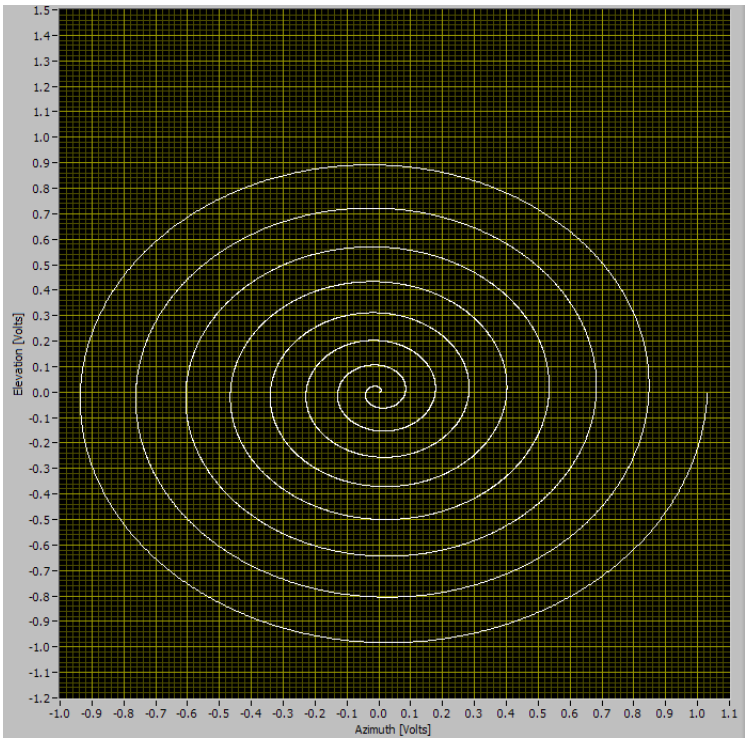

Figure 29. PAM spiral scan.

4.4.3 Frequency Response

Before mounting the FSM and PAM onto the optical breadboard, their frequency responses were evaluated. This was facilitated by use of the Newport LDS1000 autocollimator and the HP 3562A Dynamic Signal Analyzer. The HP 3562A was used to sweep a sinusoidal source over a range of frequencies for each axis. The range of frequencies tested was from 10 Hz to 2 kHz. The upper limit was chosen due to the fact that the autocollimator has a 2 kHz bandwidth. The sinusoid was swept at a rate of 21.9 Hz per second.

The source amplitude for both the FSM and PAM were different. Since the recommended input range for the FSM is from 0 to 10 V, the source was given a 5 V DC offset. The amplitude was set with a 100 mV peak. The PAM has a different input range, from -10 V to 10 V, therefore no DC offset was added to the source. The signal amplitude was reduced to 20 mV peak for the PAM.

The output of the autocollimator was wired to the input channel of the HP 3562A. The Dynamic Signal Analyzer plotted in real-time a power bode plot of the mirror response. The plot was transferred to a PC through existing LabVIEW software over a GPIB connection. The data was then plotted in Matlab and analyzed in order to understand the optimal operating frequencies of both the FSM and PAM in ALT-COM. The test setup is shown in Figure 30.

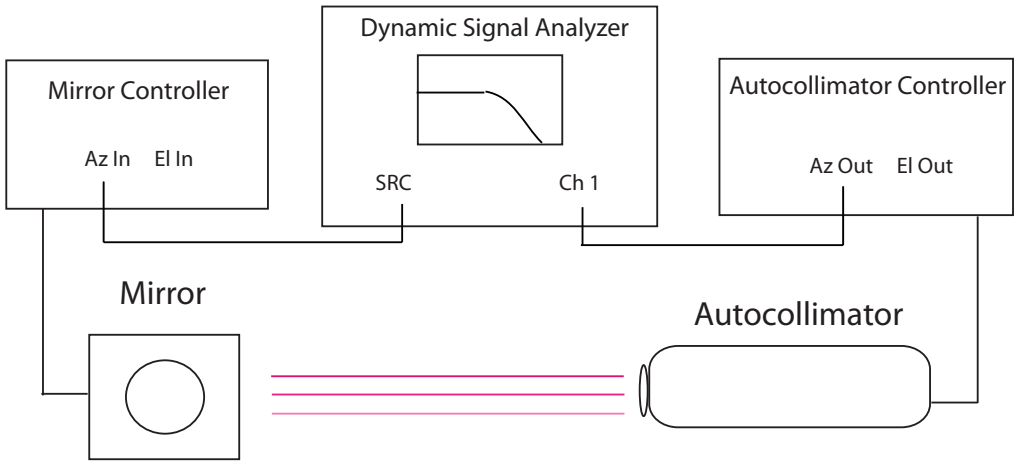

Figure 30. Mirror frequency response test setup for Az measurement (El test identical but wires switched).

The PAM was tested with an input sinusoid of amplitude 20 mV. The frequency response of the mirror is shown in Figure 31. Both inputs increase in power for the majority of the spectrum. The inputs increase in signal power by 3 dB at around 300 Hz. The frequency response provided by the manufacturer, tested with our actual mirror, shows as increase of 1 dB at around 200 Hz, however their measurements were in signal amplitude and not power. After 500 Hz in our frequency response the El input shows a sharp roll-off. The roll-off for Az is much less severe. At 1 kHz both inputs have a sharp roll-off due to the upper band limit of the autocollimator. The response

obtained is not reliable due to the bandwidth limitations of the autocollimator. The manufacturer specification of a 600 Hz bandwidth will be used during design and testing.

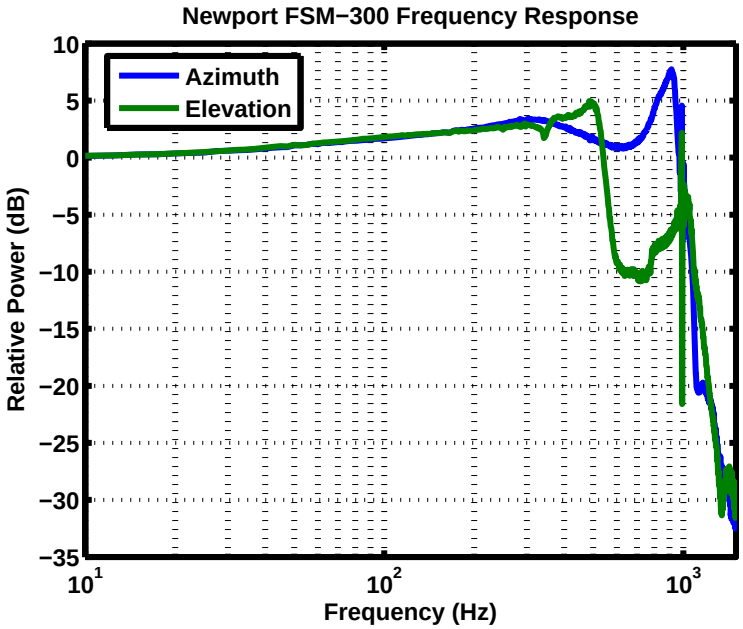

Figure 31. Newport FSM-300 frequency response.

Both azimuth and elevation inputs of the PI Tip/Tilt Platform were evaluated independently. The signal applied to each input was 100 mV peak sinusoid. The frequency response with internal feedback enabled is shown in Figure 32. With feedback enabled the open-loop bandwidth is reduced as expected. Attenuation occurs earlier in the spectrum as a result of the negative feedback, internal to the mirror, moving the pole of the system farther into the left-hand plane of the s-plane. This pole causes 20 dB/decade attenuation starting at 30 Hz. The power is cut in half at 70 Hz with internal feedback enabled, as opposed to 336 Hz for El and 409 Hz for Az without internal feedback (as shown in Figure 33). In both plots there is a drop in power at 1 kHz, this is due to the upper band limit of the autocollimator at 1 kHz.

4.5 RECEIVE PATH

At this stage the PAM was installed on the breadboard as well as the receive path. The inputs to the PAM were commanded with 0 V in order to keep the mirror centered on both axes. The first polarization beam splitter (PBS) was added to combine the transmission and receive paths. A second PBS was used in order to split the transmit beam between the receive fiber and the quad-cell. The receive fiber was then adjusted in order to properly couple the beam.

An angled physical contact (FC/APC) fiber optic was run from the Rx FLA to a power sensor. An angled fiber was required to minimize power fluctuations noticed from using a standard

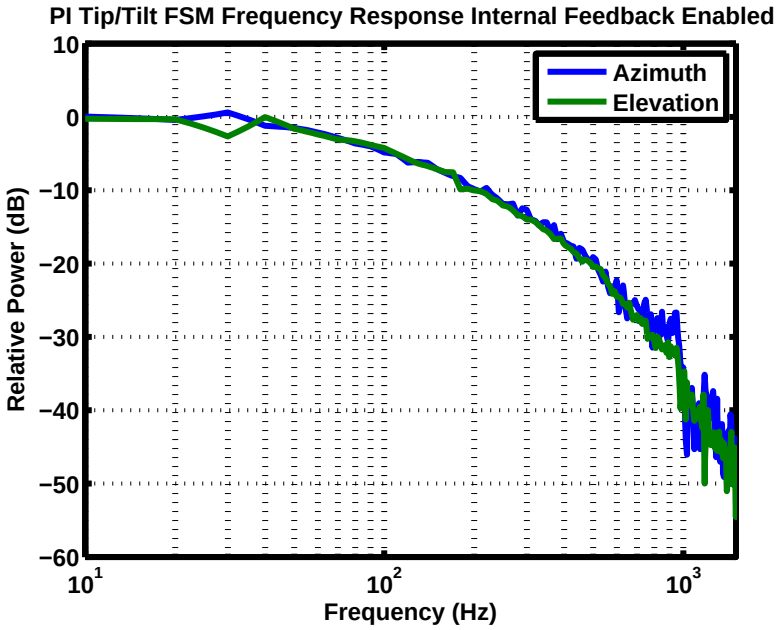

Figure 32. FSM frequency response (internal feedback enabled).

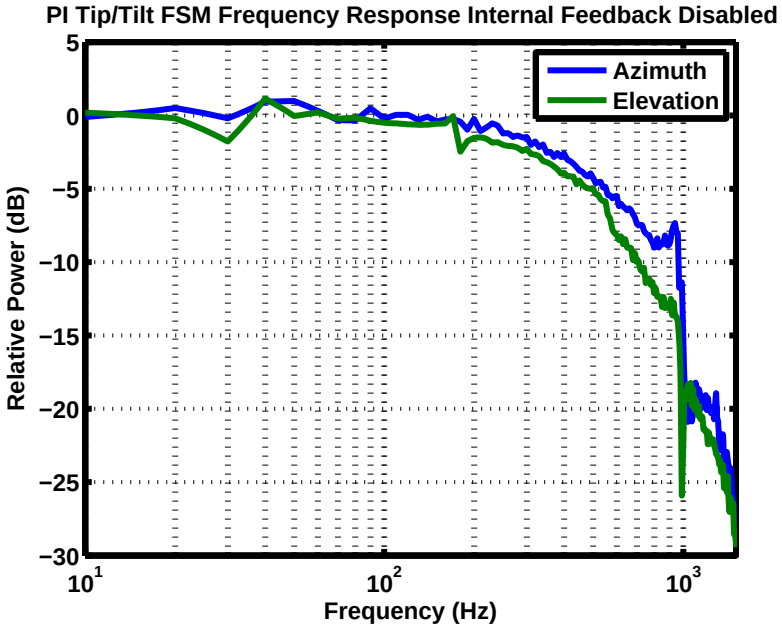

Figure 33. FSM frequency response (internal feedback disabled).

FC/PC connector. These fluctuations were roughly noted to be on the order of 0.2 dB. This introduced a need to align the beam to strike the fiber at a particular angle, which was calculated to be approximately 12°, while taking the refractive index of the fiber to be 1.5 (that of glass); this situation is demonstrated in Figure 34. The addition of a rotational degree of freedom in setting the fiber, however, increased difficulty in alignment resulted in an overall reduction in optical power coupled into the fiber.

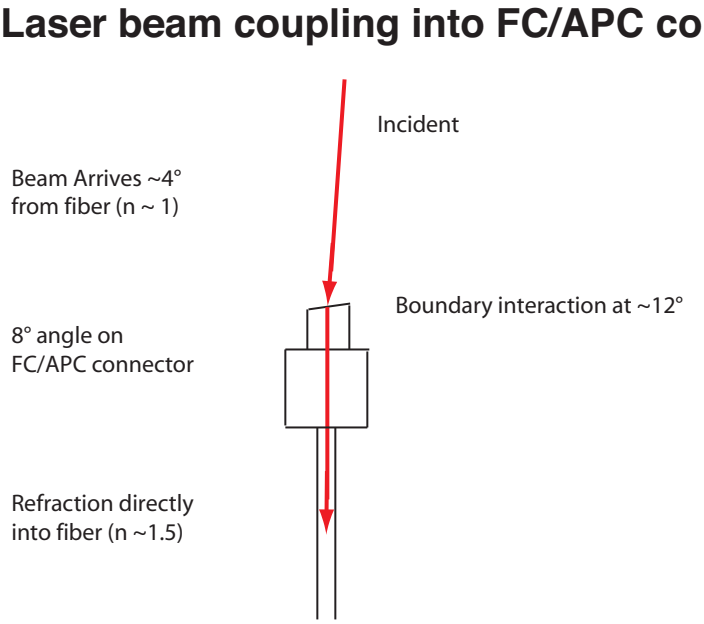

Figure 34. Coupling into an angled connector.

Alignment was done in a series of steps. Firstly, the second PBS was placed with the eventual position of the Rx FLA in mind; light from the PBS was required to illuminate the fiber without the focusing lens in place. A power meter or an infrared card helps with this task. Secondly, the lens is place roughly by hand. The lens focal length (22 mm) was used to guide the distance, and the light was checked to pass through the center of the lens. Again, the power meter and infrared card are great aids to this. The stage tilt in the X-Z plane was also roughly aligned by using an angle cut from an index card as a reference.

From this point, fine alignment is obtained through FLA stage and lens mount adjustments. One useful technique was to launch a beam through the Rx FLA. This way, a small mirror could be temporarily placed so that this beam, once passed through the lens, is diverted to the WFS. At this point, it should be possible to collimate the beam such that it can be expected that another collimated beam would focus very near the core of the fiber. Additionally, as additional laser sources were available and previously unused, lasers could be sent from both the Tx and the Rx FLAs simultaneously. Ideally, both beams are collimated and are collinear with each other. A

TABLE 10

Fiber Coupling Loss Breakdown

Loss Mechanic	Loss Measured (dB)
Strehl Losses	0.13
Fresnel Reflections	0.18
Misalignment	4.02
Total Loss	4.34

TABLE 11

Test-Beam From Rx FLA

Characteristic	Value
Wavefront Error	0.067 waves rms
Strehl Ratio	0.838
Beam Diameter ($1/e^2$)	3.318 mm
Beam Divergence ($1/e^2$)	0.8376 mrad

Wavefront error stated at $\lambda = 1.55\ \mu m$.

double-sided infrared card is an excellent check, if it can illuminate to show both lasers on each side.

Finally power measurements are taken before the lens and from the power meter connected to the Rx FLA. The difference in dB is taken to be the insertion loss, which had a target value of 2 dB or less. Table 10 shows investigation into the insertion loss. Strehl losses arise from wavefront error, which limits the peak intensity in focusing Gaussian beams [10]. Additionally, Fresnel reflections were investigated as an additional source of loss. It must be noted that the light coupling into the fiber is S-polarized as it was last reflected from a PBS [4]. The remainder is attributed to poor alignment which may be increased with more precise stages. In particular, the staging mounts for ALT-COM lacked direct control of relative positions along the Z-axis. This suggests that this loss could be diminished greatly with very little design alteration.

This alignment was further characterized by using the Rx FLA to send light from a similar laser source through the lens. This beam was then characterized and compared to the communication beam. The results summarized in Table 11. The wavefront error, while considerably higher than the communication beam, is still regarded as well-corrected [13]. This investigation shows us that the lens itself is not of such low quality as to cause this amount of loss. The average beam size is smaller than the communication beam, which resulted in a higher divergence. However, not shown well in the table is a comparison of ellipticity. The beam from the Rx FLA had divergences of 0.93 mrad in one axis and 0.75 mrad in the other. In comparison, the communication beam had divergences of 0.57 mrad and 0.59 mrad along its axis. This further suggests that the insertion loss in the Rx FLA may be due largely in part to misalignment. The beam size did not immediately appear to be elliptical.

Figure 35 shows the wavefront of the test beam from the Rx FLA. The beam has a gradient in its wavefront error, giving a sense that the wavefront is curved. As discussed earlier in Sec 4.3.4, this indicates that the lens and fiber are not at a distance of one focal length apart, resulting in a divergent beam. Fine alignment along the focus was difficult, as both the lens mount and Rx FLA lacked independent control over that distance.

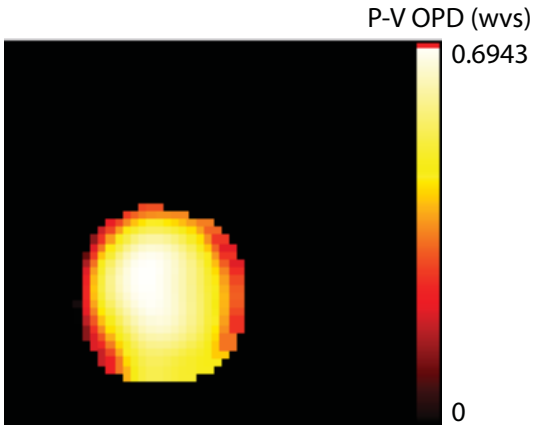

Figure 35. Test beam from Rx FLA.

4.6 DESIGN INTERFACE BETWEEN FSM AND QUAD-CELL

In order to maintain tracking during laser communication the beam must be directed at the proper angle from the FSM. The fast-steering mirror adjusts the angle of reflection based on the control signal provided by the quad-cell. The quad-cell controller provides two signals which must be interfaced with the FSM controller. The signals provide information on the elevation and azimuth of the beam seen on the quad-cell. The tracking control loop is shown in Figure 36.

The quad-cell that was used in ALT-COM is an existing in-house built component whereas the FSM was a new commercial component. The output signals of the QC controller were conditioned such that the FSM controller could read the signals and adjust the FSM appropriately. The quad-cell controller signals are connected to an external board, known as the gimbal tracking interface, that integrate the error in the position of the beam on the quad-cell. The gimbal tracking interface circuit was modified in order to interface the FSM and quad-cell. The modified gimbal tracking interface circuit is shown in the Appendix in Figure 55.

4.6.1 Orientation of Quad-Cell Head

Before interfacing with the quad-cell the head needed to be oriented in the desired direction. The orientation of the axes were determined as well as the sign of the outputs. The gimbal tracking interface (external board used to integrate the error signal) can be modified in order to change the sign of the output. The quad-cell head is currently used in the Tracking Testbed in the upright

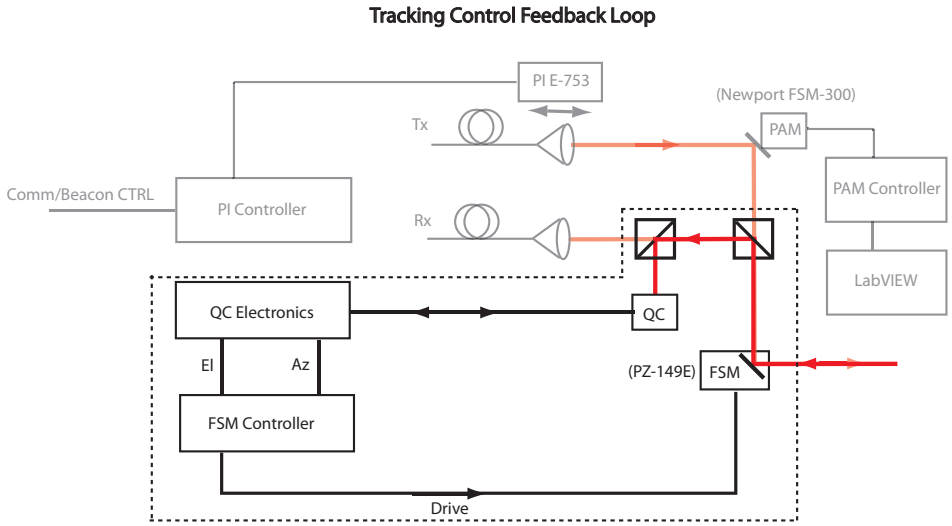

Figure 36. Tracking feedback loop.

orientation as shown in Figure 37. With an inverting amplifier on the quad-cell elevation output, and a non-inverting amplifier on the azimuth axis, the controller outputs are as shown. The azimuth and elevation outputs directly correspond to the physical orientation of the quad-cell. For ALT-COM the quad-cell was rotated 90° to mount it at the proper beam height. This caused the quad-cell elevation axis to become the ALT-COM azimuth axis, and the quad-cell azimuth axis to become the ALT-COM elevation axis. The final signs of the axes are as shown in the figure. With the quad-cell cable facing toward the left, a beam primarily on the left side of the cells causes a positive output. This output causes the FSM to correct its position, moving the beam farther to the right of the cells. The next section will describe, in detail, the circuit modifications made to the gimbal tracking interface to obtain these signed outputs.

The gimbal tracking interface includes five op-amps in the path from input to output. The operation of these op-amps are configurable by applying TTL signals to select test pins on the board. The first op-amp, which is not configurable through the switch, acts as an inverting amplifier with unity gain at DC. The second op-amp is the first integrator in the path. This integrator is enabled by setting test pin 10 (labeled first-order) to a logic 0. This breaks the connection between two resistors in the feedback loop, causing the output to hit the ±12 V rail depending on the polarity of the input signal. The third op-amp can also act as an integrator, and can be enabled in conjunction with the first integrator to create a second order integrator. For ALT-COM this integrator will be disabled by setting test pin 3 (labeled 2nd order) to 0 V. By setting this pin to 0 V, the analog switch bridges two resistors causing the op-amp to act as an inverting amplifier with unity gain at DC. The final two op-amps (shown after the analog switch in the circuit) allow selection of inverting or non-inverting unity gain at the output, in order to assign the correct polarity for the particular use.

The gimbal tracking interface, acting as a first-order integrator, outputs ±12 V. However, as the FSM requires an input between 0 and 8 V, the gimbal tracking interface circuit needed

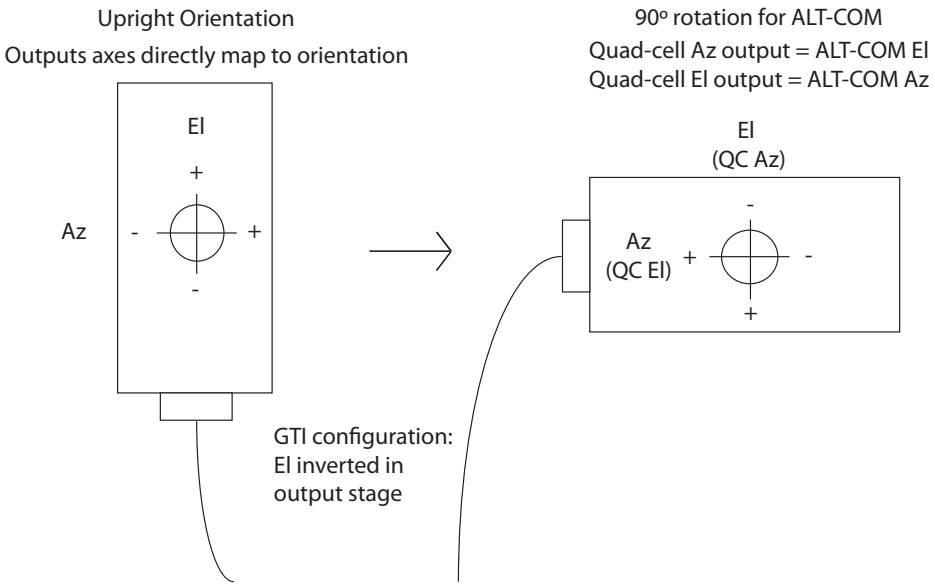

Figure 37. Quad-cell head orientation.

to be modified. The first modification was to select the proper output op-amp after the analog switch (to select the proper sign of the output). Based on the orientation of the quad-cell head, the azimuth output of the quad-cell (system elevation axis) had to be inverted by enabling the unity gain buffer. The quad-cell elevation axis (system azimuth axis) was connected with the unity gain inverting amplifier in the output stage. The second change made to the circuit was adding a 1N4153 diode in parallel with C29 (in the El path) and one in parallel with C19 (in the Az path). The cathode of the diode is connected to the output of the op-amp for the El path, whereas the anode is connected to the output of the op-amp for the Az path. This is due to the sign difference in the output of the paths. With the first-order integrator enabled and the diode in place limiting the direction of current, the output of the elevation integrator was not allowed to hit the -12-V rail. The elevation integrator was not allowed to hit the 12-V rail. With these modifications the outputs of both paths were limited from -0.9 V to 12.2 V. In order to obtain the desired output range of 0 to 8 V, the gain of the second order integrator op-amp in the path (not used as an integrator in our application) was modified. As opposed to the current gain of one achieved with two 10-kΩ resistors, one resistor was changed to 15kΩ in order to decrease the output from a nominal 12 V to 8 V.

4.6.2 Installation of FSM and Tracking Feedback Loop

The FSM was mounted onto the optical breadboard and optical alignment was performed. Since the control voltages for the FSM controller are between 0 and 8 V, the beam was aligned with 4 V applied to each input of the controller. This was done to allow the maximum amount of angular range when configuring the tracking feedback loop (TFL). Next the quad-cell head was mounted on the board with a stage for fine adjustment in x, y and z. Coarse alignment was performed by checking the position of the beam on the quad-cell. Without feedback enabled, the quad-cell

controller was powered on, and the stage was adjusted until the error for both Az and El was close to zero. The output of the quad-cell controller was then fed to the FSM controller inputs, enabling feedback. The quad-cell stage was then adjusted in Az and El until the input voltages read on the FSM controller display were close to 40 V on both axes (this converts to a 4 V input due to the 10x internal gain of the controller).

4.7 CHARACTERIZE TRACKING FEEDBACK LOOP AND FSM

In order to evaluate the bandwidth of the tracking feedback loop the transfer function of the components in the loop must be found. The loop is comprised of the quad-cell head/controller, the gimbal tracking interface (GTI), the FSM controller, and the FSM mirror. Each of these components has a transfer function that affects the loop transfer function as shown in Figure 38. Assuming these each of these components are linear and time-invariant, we can find the transfer function of each component and determine the transfer function of the tracking feedback loop. In the time domain these transfer functions can be convolved to find the system transfer function, or in the frequency domain they can be multiplied. The simplest method is to find the component transfer functions in the frequency domain on a logarithmic scale. The magnitudes of each components can be added according to Equation 4. The phases can also be added, as they are the imaginary element of the logarithmic complex transfer function.

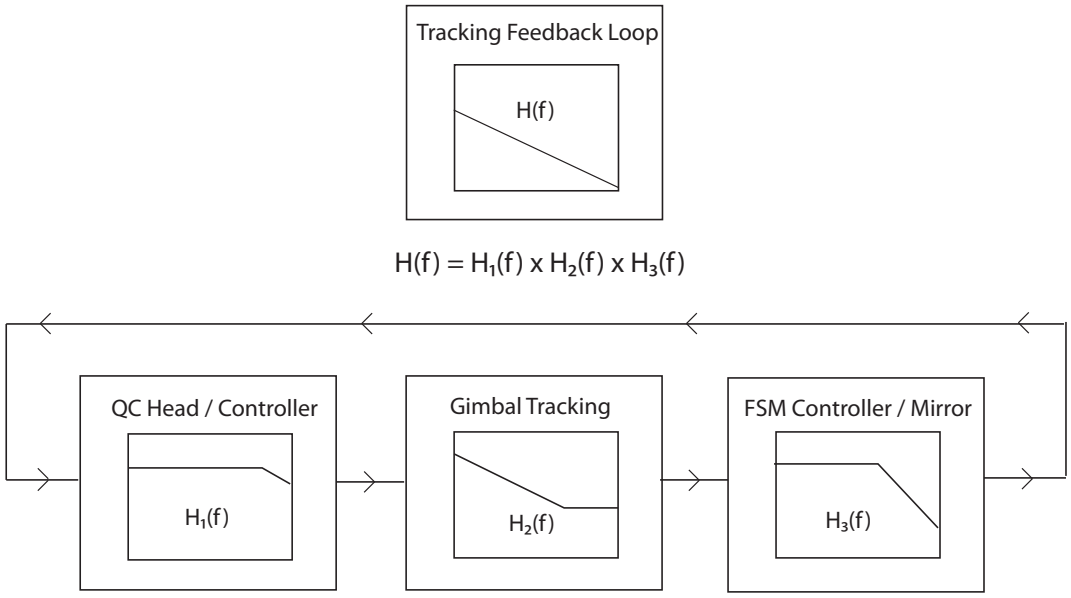

Figure 38. Contribution of individual components to loop transfer function.

$$log(ab) = log(a) + log(b) \tag{4}$$

The HP Dynamic Signal Analyzer, Model No. 3562A, was used to determine the transfer functions of each components in the tracking feedback loop. The DSA plotted both the magnitude and phase of the tested component's transfer function. A LabVIEW program, developed by the members of the Advanced Lasercom Systems and Operations Group, was used to transfer the graph data to a PC through a GPIB connection. The program yielded an Excel sheet containing the data for both the magnitude and phase plots. The system was first tested with a unity gain first-order integrator in the gimbal tracking interface, and then the loop bandwidth was examined and adjusted by tweaking the gain of the integrator.

The frequency response of the quad-cell head and controller tested by use of an red LED. The LED was placed in front of the quad-cell head and the intensity of the light was varied by changing the voltage appearing across the diode. This was facilitated by use of the DSA. The sinusoid was swept from 1 Hz to 1 kHz, and the power output of the quad-cell controller was monitored. The LED circuit is shown in Figure 39.

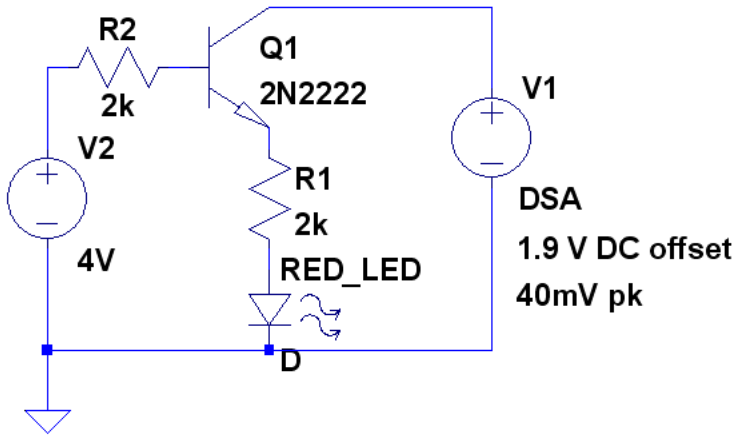

Figure 39. LED circuit used to test frequency response of quad-cell head and controller.

The base of the transistor was powered by a DC power supply with constant 4 V. This completed the connection of the DSA swept sinusoid voltage through the diode to ground. The sinusoid was biased at 1.9 V, the forward bias of the diode, and varied by 40 mV in order to change the intensity of the light.

It is important to note that this test used an LED with varying intensity, as opposed to a jittered beam, to eliminate the superposition of the PAM frequency response in the found quad-cell response. The quad-cell response is shown in Figure 40.

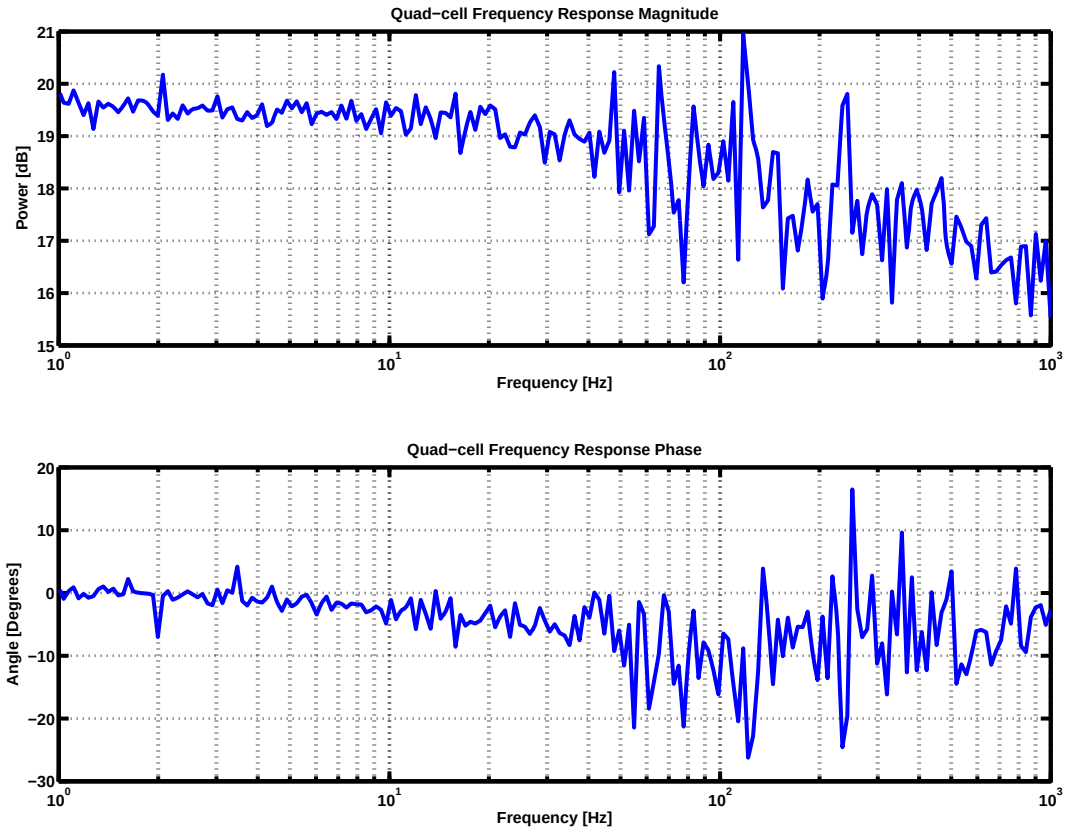

Figure 40. Quad-cell frequency response magnitude and phase.

The quad-cell frequency response magnitude starts to attenuate at 20 Hz and continues out until 1 kHz, however the attenuation is only about 1.5 dB/decade. The phase drops about 10 degrees during that interval. The quad-cell has a relatively flat bandwidth out to 1 kHz.

The frequency response of the FSM/controller was tested using the setup shown in Figure 41. The FSM was tested over the same frequency range as the gimbal tracking interface. Feedback from the quad-cell was removed for this test in order to determine the open-loop response of the mirror. The frequency response of the mirror was retested with the quad-cell, as opposed to the autocollimator in Section 4.4.3, since the quad-cell head/controller bandwidth is 1 kHz. Each axis of the FSM was tested independently through use of the DSA. The test axis was driven by the DSA with a 40 mV peak sinusoid with a 4 V DC bias. This bias was necessary since the laser beam was aligned to the FSM with a 4V input bias on each axis (4 V is the middle voltage in the angular range of the mirror). The axis that was not being tested was given a constant 4 V by an Agilent DC Power supply, Model No. 3631A. The source to the FSM controller was also split to the first input channel of the DSA while the output of the quad-cell was connected to the second input channel.

The frequency response of the FSM is very similar on both the azimuth and elevation axes. The response for both axes in magnitude and phase is shown in Figure 42. There is a considerable amount of noise in the lower frequencies, which is centered about 15 dB of attenuation. The response then starts to drop at about 5 dB per decade around 30 Hz, with about 3 dB loss at 180 Hz (overlooking the noise deviations). This cutoff frequency is very different from the cutoff near 350 Hz found in the autocollimator test. The phase response shows a 180 degree shift at 1 kHz.

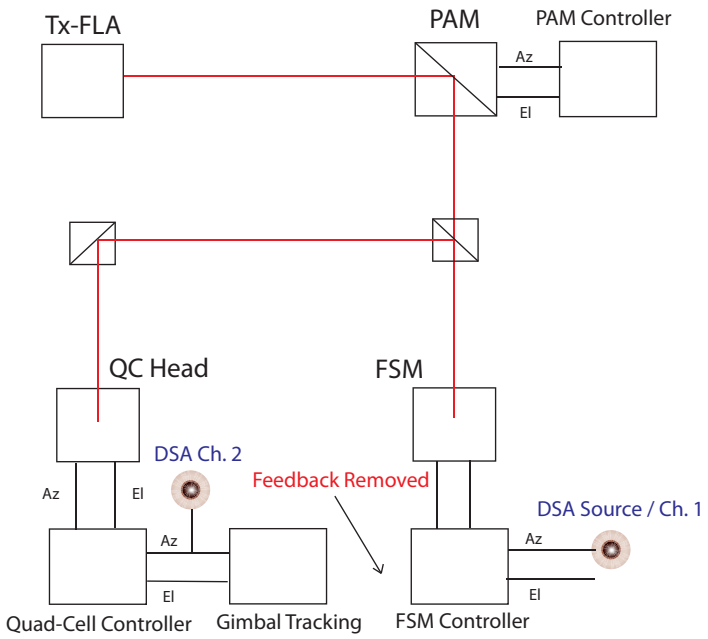

Figure 41. Setup used to test FSM frequency response.

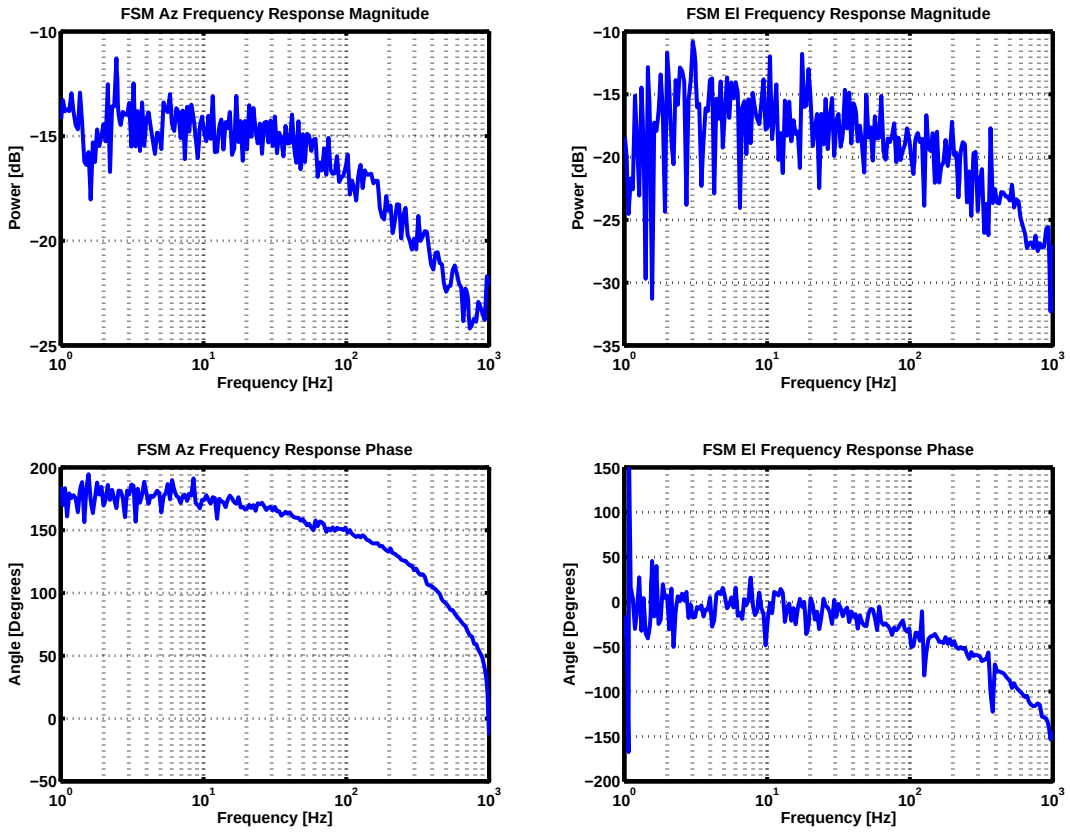

Figure 42. Frequency response of the PI FSM tested with the quad-cell.

The frequency response of the gimbal tracking interface was tested using the setup shown in Figure 43. This figure shows testing of the gimbal tracking interface in the azimuth axis. Independently each PAM axis was driven by the DSA with a 40 mV peak sinusoid. The sinusoid was swept logarithmically from 1 Hz to 1 kHz at a rate of 22.7 seconds/decade. The second channel input of the DSA was connected to the axis output of the quad-cell controller, and the first channel was connected to the axis output of the gimbal tracking interface.

The gimbal tracking interface was first tested with a unity gain first-order integrator. The frequency response of the GTI is shown in Figure 44. The expected cutoff frequency is 159 Hz due to the parallel combination of the resistor and capacitor in the feedback loop. The plot shows that at frequencies below the 143 Hz cutoff there is a 20 dB/decade attenuation. This is due to the first-order feedback in the integrator. The response starts to flatten after 143 Hz.

In the phase response the pole of 143 Hz increases the phase, until the zero starts to level the phase at 143 Hz. The zero is caused by the additional capacitor in the feedback loop in series with the parallel resistor and capacitor.

This test had the potential for inaccuracies in using the PAM to dither the beam. However, since the gimbal tracking interface is bandwidth is below the 600 Hz bandwidth of the PAM, the PAM frequency response has no effect on these test results.

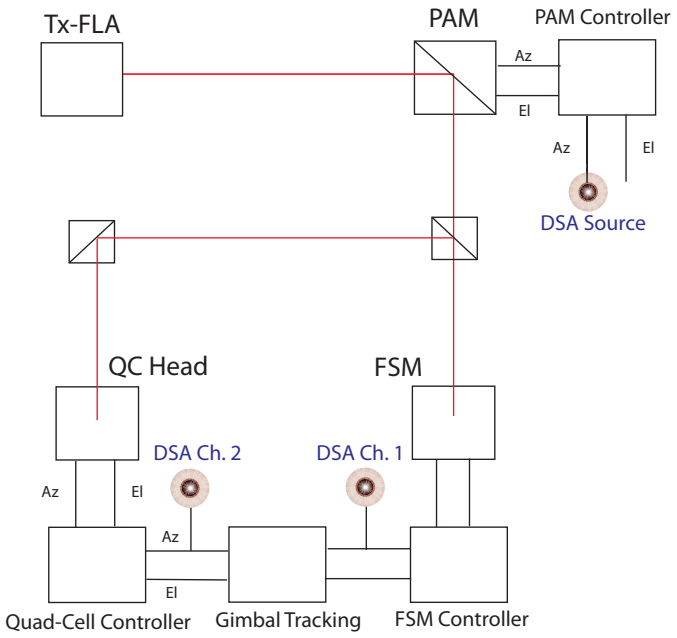

Figure 43. Setup used to test gimbal tracking interface frequency response.

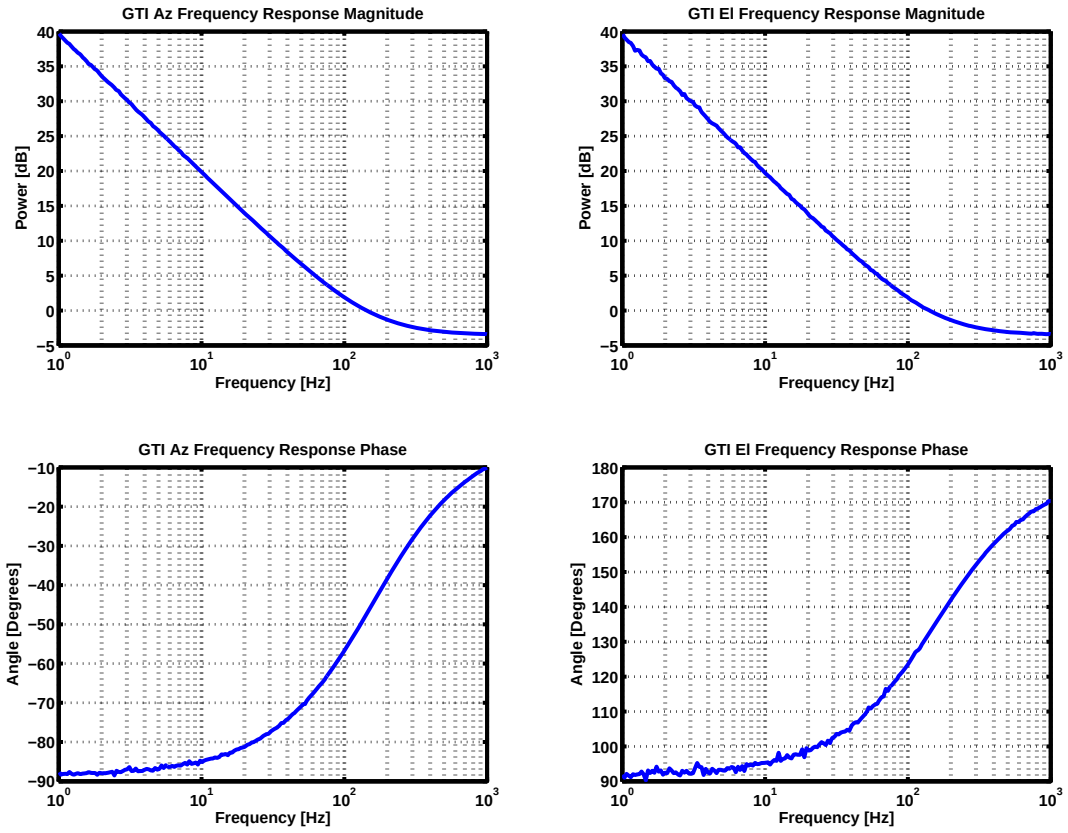

Figure 44. Frequency response of the GTI with 1x gain.

4.7.1 Frequency Response Analysis

After collecting all of the Excel sheets for these tests, a Matlab script was written to extract the magnitude and phase data for each component. The script then added the component magnitude plots for both azimuth and elevation axes. The frequency response of the quad-cell was not summed with the rest of the responses, as the FSM frequency response inherently includes the quad-cell head/controller response (the quad-cell head/controller was the test apparatus for the FSM test). Similarly, the phase plots for the components were summed. The magnitude and phase plots for the tracking feedback loop were then graphed, showing the response for both axes. These plots were analyzed in order to determine the tracking feedback loop bandwidth and stability.

The tracking feedback loop was initially viewed with the unity gain first-order integrator in order to determine the bandwidth of the feedback loop. The response of the loop is shown in Figure 45. The responses are very similar for both azimuth and elevation axes. Close to DC the power is at 25 dB and then drops at 20 dB/decade from the integrator contribution to the loop. At 143 Hz the zero from the integrator starts to counteract the integrator pole, however the tracking feedback loop continues to attenuate after this frequency due to the FSM pole. The attenuation per decade after 100 Hz is less than lower frequencies because the FSM pole causes about 5 dB/decade attenuation.

The phase response of the tracking loop is relatively flat until 200 Hz. From 200 Hz to 1 kHz there is a 90 degree phase shift. This is due to the pole of the FSM. The FSM pole overcomes the contribution of the zero from the GTI.

The important information to take from this response is the bandwidth and stability of the tracking feedback loop. A stable system has poles in the left-hand plane of the s-plane. Poles in the right-hand plane cause the system to be unstable as a positive σ in $e^{\sigma+j\Omega}$ causes an exponential rise.

In order to determine system stability, the 0-dB point of the magnitude response must be examined. This is the point at which the magnitude of the gain times the loop gain is 1. The phase at this point must be at least 45 degrees away (45 degree phase margin) from -180 degrees in order for the system to have a reasonable amount of stability. With a unity gain integrator the 0 dB point is at 20 Hz. The phase margin at this point is 270 degrees. Since this value is much greater than 45 degrees, the bandwidth of the loop can be increased without affecting the stability of the system.

To increase the bandwidth of the tracking feedback loop the integrator was modified. The 10 kΩ resistor on the inverting input of the integrator (for both axes) was replaced with a 500 Ω resistor to give the integrator a gain of 20, in hopes of extending the bandwidth to 400 Hz. This configuration was tested, however was unsuccessful as the piezo FSM began to resonate. This resonance is visible at 400 Hz in Figure 42. The resistor was then replaced with a 1 kΩ resistor. This setup was tested and initially successful, as the FSM did not resonate. The frequency response of the 10x integrator is shown in Figure 46. The gain at DC increased by a decade from 40 dB to 60 dB (the 10x gain that was expected).

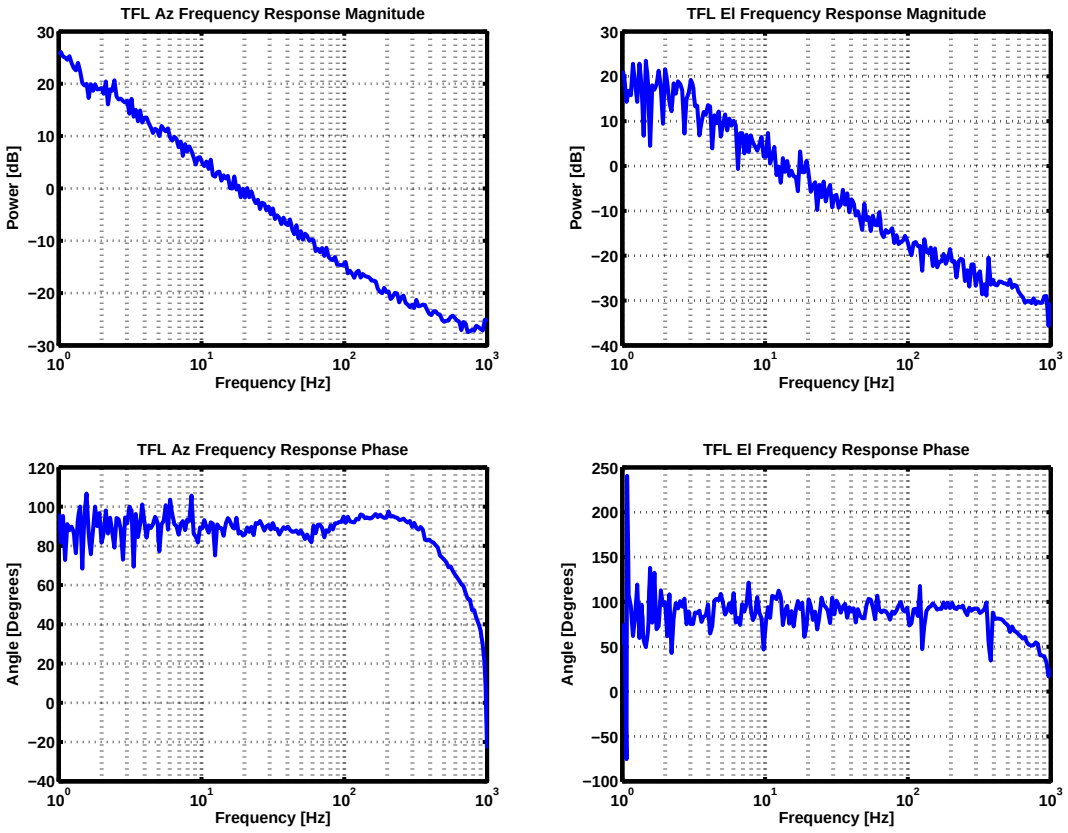

Figure 45. Frequency response of the TFL with 1x gain.

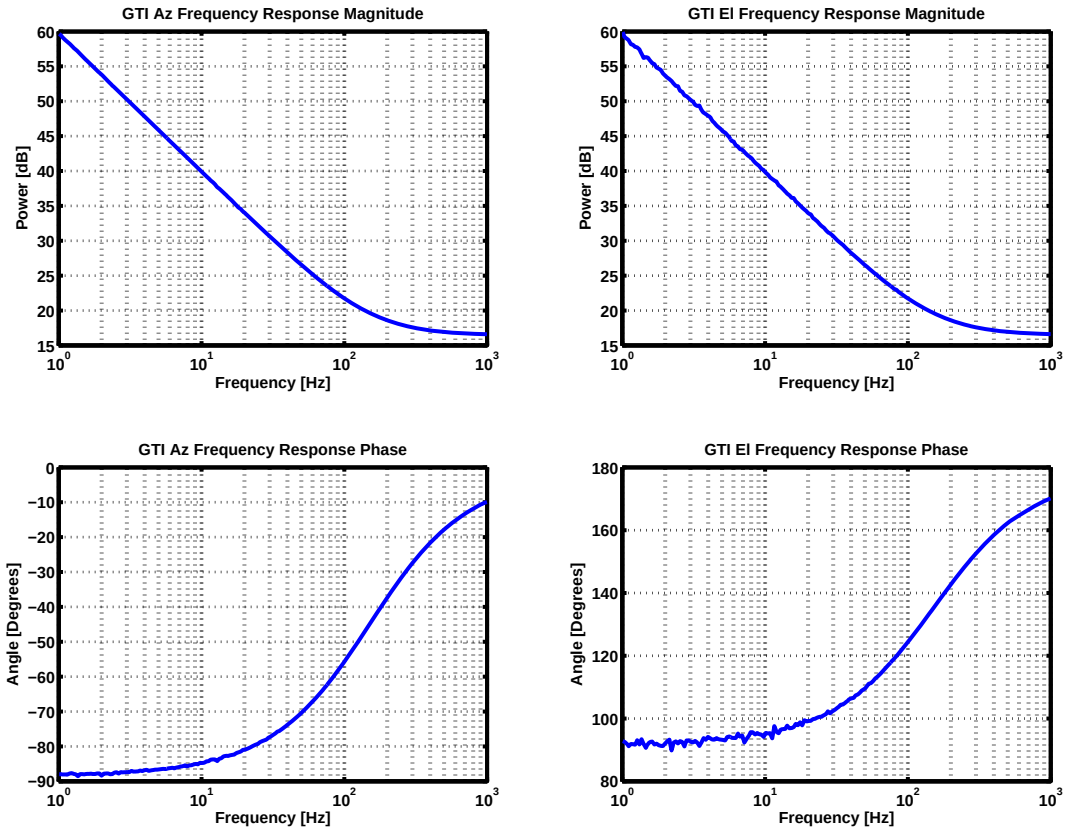

Figure 46. Frequency response of the GTI with 10x gain.

With the change in gain on the integrator the frequency response for the TFL had to be redetermined. Although the FSM frequency response was not affected by the change in the integrator, the response was tested again for comparison against the first trial. The new plot was essentially the same as the first trial, however there was more noise in the lower frequencies. This new plot was used in finding the frequency response of the tracking feedback loop. The new frequency response of the loop is shown in Figure 47. As expected the bandwidth of the tracking feedback loop increased to 200 Hz. Although it appears that there is 270 degrees of phase margin, and enough gain margin to increase the TFL bandwidth, the FSM El resonance close to 400 Hz limits our margin for improvement. With any additional gain the resonance will cross unity gain and the drop in phase will be pushed closer to -180 degrees. This will cause instability in the tracking feedback loop. Further investigation can be done on this resonance by running a linear sweep from 300 Hz to 600 Hz.

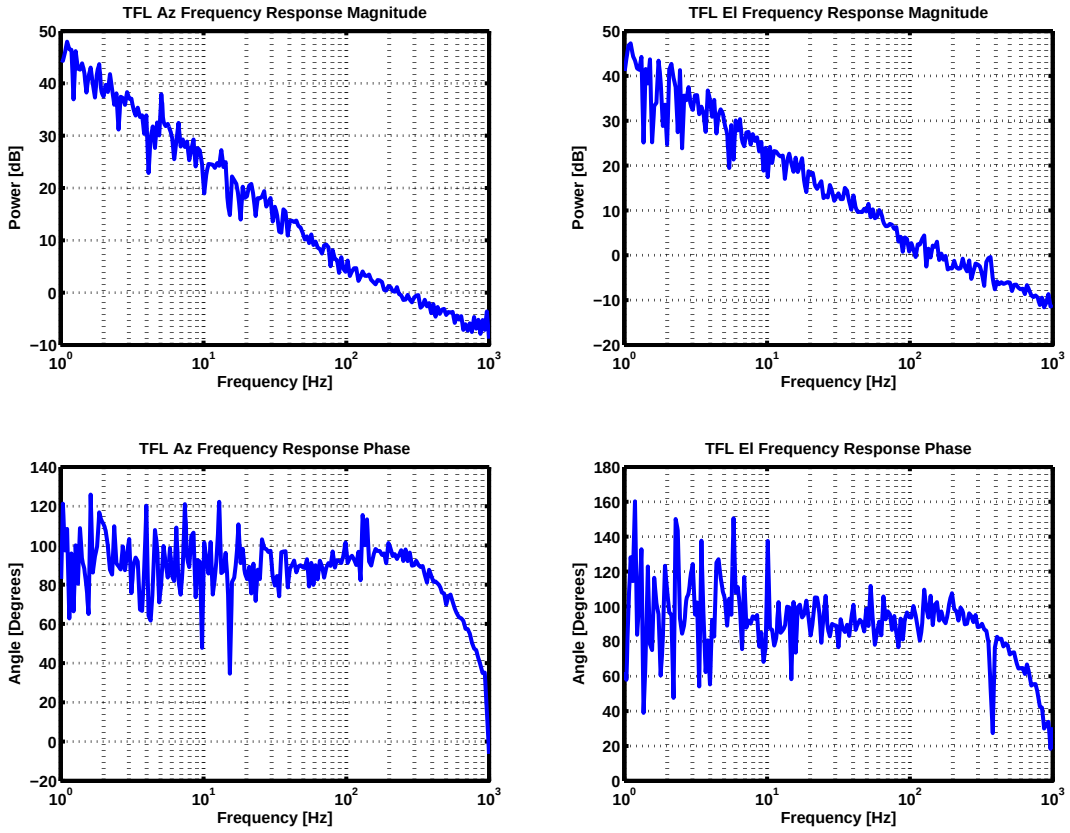

Figure 47. Frequency response of the TFL with 10x gain.

The rejection frequency of the tracking feedback loop was tested using the setup shown in Figure 48. In this setup the PAM test axis was sourced by the DSA, and that line was split to

the channel one input. The TFL was monitored with channel two of the DSA on the test axis between the QC controller and GTI. The desired graph from this test was to look like a high pass filter response. The rejection frequency is the 3 dB point before the response flattens out. This frequency should match the cutoff frequency found in the TFL frequency response. The response seems to flatten and settle at a value for the unity gain GTI plot, as shown in Figure 50. The asymptotes are close to 10.5 dB for Az and 7 dB for El. Based on these values we can expect the rejection plot with 10x GTI to settle at the same values. The resulting plots for both azimuth and elevation axes with 10x GTI are shown in Figure 49. The response does not flatten as the unity gain response does, however, we can superimpose the asymptotes from the unity gain GTI plot in order to determine the rejection frequencies. Note that the power units are arbitrary as the output voltage of the quad-cell has not been mapped to angular movement.

The rejection frequency is 3 dB below the asymptote. The cutoff frequency is around 200 Hz for both plots which directly corresponds to the bandwidth found in the TFL frequency response test. The frequency response and rejection plots have been verified as correct.

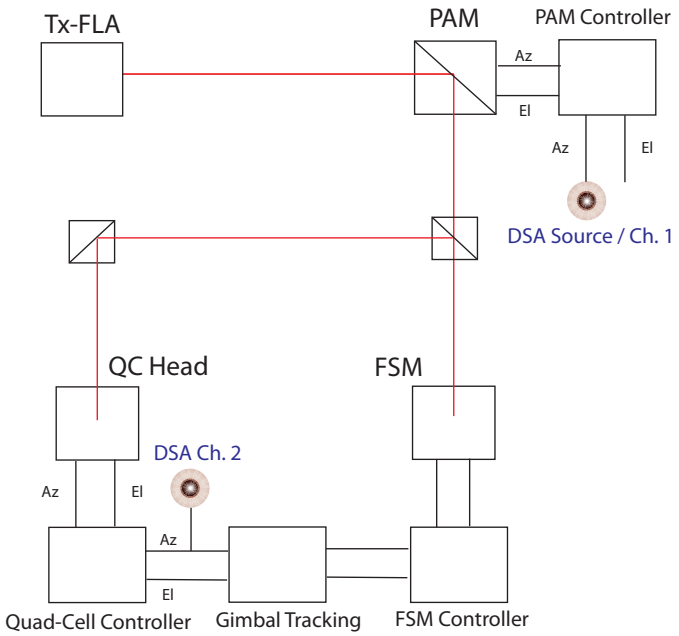

Figure 48. Setup used to test TFL rejection frequency.

4.7.2 Jitter Rejection

A LabVIEW program, used in the Tracking Testbed for simulating platform jitter, was used to test the performance of the tracking feedback loop. Performance was tested with three jitter profiles (0.5, 1.5, and 4 in beams). The test involved measuring the jitter power spectral density from the output of the quad-cell controller with tracking enabled and disabled (residual jitter and applied jitter). The DSA was used to create the PSD, and then the graphs were transferred to a

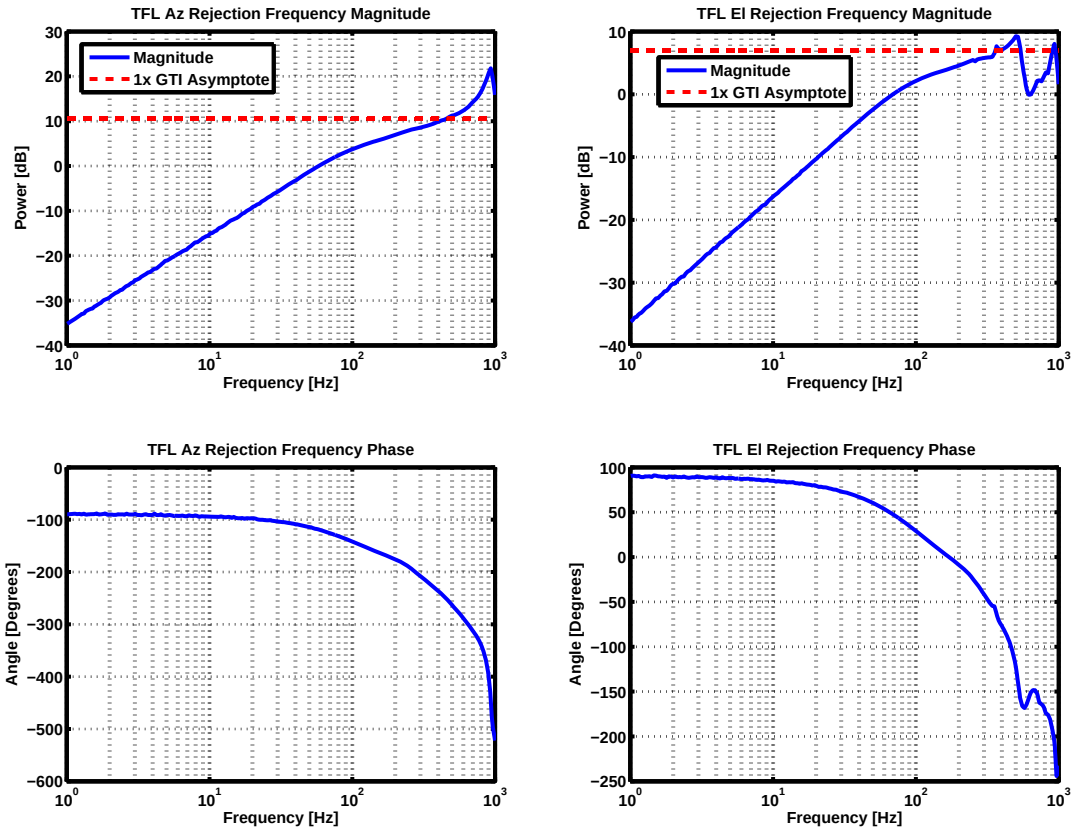

Figure 49. Rejection frequency of TFL with 10x GTI.

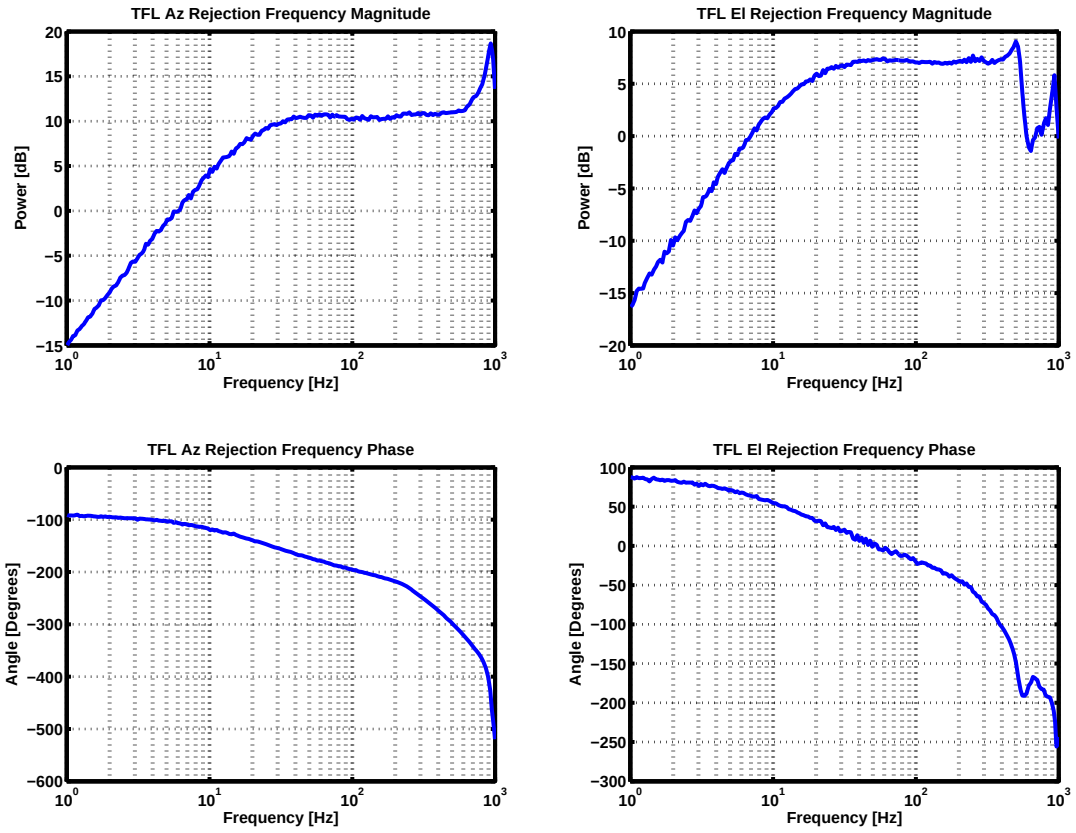

Figure 50. Rejection frequency of TFL with 1x GTI.

TABLE 12

Platform Jitter Parameters

Beam Size (inches)	Az Input (μrad/V mech.)	El Input (μrad/V mech.)
0.5	2930.7	2777.7
1.5	976.9	925.9
4	366.3	347.2

PC through a GPIB connection. Once the data was transferred to the computer, a Matlab script was written to compute the amount of jitter in comparison to the beamwidth.

In order to setup the test for the three platform jitter models, the input parameters to the LabVIEW program needed to be determined. With default parameters, the voltage slopes of the PAM, 2930.7 μrad/V for Az and 2777.7 μrad/V for El, the program provides platform jitter for the 0.5-in beam model. The slopes were then scaled for the other beam models. The input parameters for the three beams are shown in Table 12.

The DSA jitter plots were taken in logarithmic units of $V/\sqrt{\text{Hz}}$ for power spectral density. These PSD values were first converted to linear units, and then the PSD was squared to obtain units of V^2/Hz. The PSD was then integrated, and a cumulative summation was done to find jitter in units of V^2 rms. Finally the square-root of the summation was taken to obtain the jitter in units of volts. In order to relate this value to the beamwidth, a calibration test was run with the quad-cell.

An Agilent function generator, Model No. 33220A, was used to control the PAM with a 1 Hz frequency, 3V peak ramp. An oscilloscope was used to view the output of the quad-cell as well as the ramp input. The ramp was large enough to steer the beam outside of the quad-cell FOV.

The traces were imported to Excel in order to see the region where the quad-cell output followed the same ramp as the control input (the QC field-of-view). Linear regression was completed for these regions in order to find the ratio of the slopes between the quad-cell output trace and the ramp input. The QC calibration factor for Az was 0.35 and 0.51 for El. These factors were then multiplied with the PAM μrad/V angular slopes and jitter values in Volts. This gave us the jitter in microradians.

The requirement for the jitter test was to have residual jitter $<$20 μrad out to 1 kHz. As shown in Figure 51, the TFL is effective at reducing the power spectral density of the applied jitter for frequencies less than 200 Hz (the rejection frequency of the TFL). The results of the 0.5-in beam platform jitter test are shown in Table 13. The applied jitter was roughly 45 μrad, and the residual jitter was around 5 μrad. The TFL brought the applied jitter, which was 30% of the beamwidth, down to 3% of the beamwidth.

For the 1.5-in beam platform jitter test, the TFL was also effective in removing the applied jitter for frequencies less than 200 Hz, as shown in Figure 52. Table 14 shows that the platform jitter was brought down from 120 μrad to 14 μrad. The applied jitter, 240% of the beamwidth, was brought down to 25% of the beamwidth. This is a significant reduction in jitter. Applied

TABLE 13

0.5-in Beam Platform Jitter Results

Jitter Conditions	Az	El	Units	Az	El	Units
Applied	43.26	47.37	μrad (rms)	27.8%	30.4%	$(4\lambda)/(\pi D)$
Residual	4.70	5.32	μrad (rms)	3.0%	3.4%	$(4\lambda)/(\pi D)$

D defined as aperture diameter.

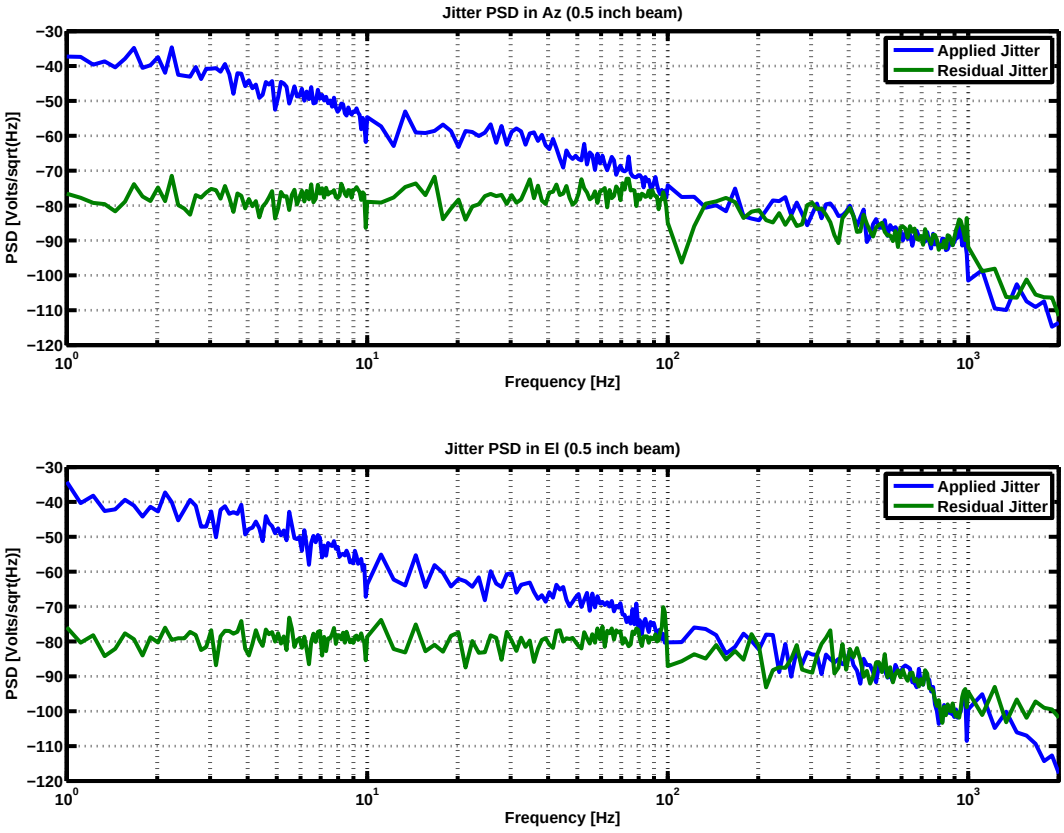

Figure 51. 0.5-in beam platform jitter PSD.

jitter, 240% of the beamwidth, causes the beam to primarily be outside of the quad-cell FOV. With tracking enabled the beam is stabilized within the quad-cell FOV. In conclusion, the 0.5- and 1.5-in beam tests the TFL satisfied the requirement of <20 μrad of residual jitter out to 1 kHz.

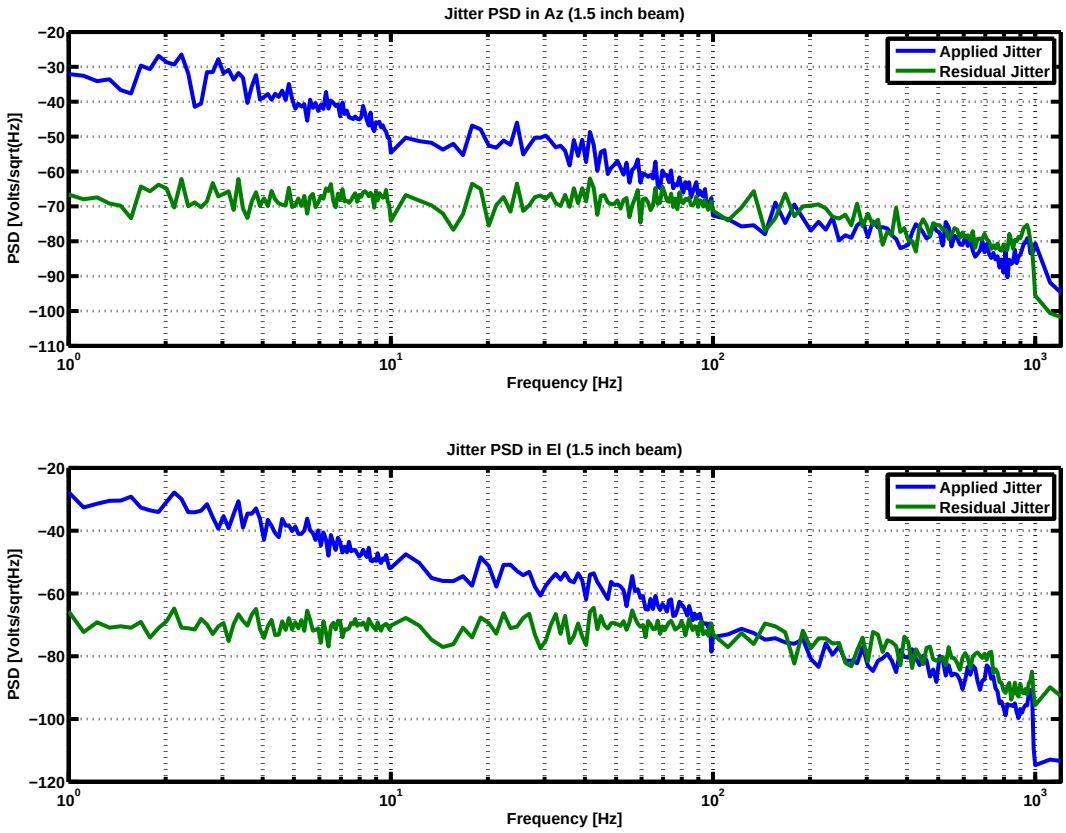

Figure 52. 1.5-in beam platform jitter PSD.

For the 4-in beam platform jitter test the TFL was more effective in removing jitter in the El axis than in Az. This is clearly visible in the PSD shown in Figure 53. In the El axis applied jitter 1897% of the beamwidth was brought down to 189.7% of the beamwidth. For Az, applied jitter 1432% of the beamwidth was brought down it only 323.8% of the beamwidth.

An additional test was run on the TFL to find the limitations in the Az axis for 4-in beam platform jitter. This was done by running the jitter test and viewing both the quad-cell controller proportional output and the GTI output control signals. Figure 54 shows both of these signals during a TFL failure. The tracking failure is caused by the GTI Az output railing to the lower output range. This voltage is at the angular limit of the FSM. Because the FSM cannot be moved an additional amount, the beam position is not corrected on the quad-cell head. This causes the

TABLE 14

1.5-in Beam Platform Jitter Results

Jitter Conditions	Az	El	Units	Az	El	Units
Applied	109.46	131.48	μrad (rms)	211.3%	253.8%	$(4\lambda)/(\pi D)$
Residual	13.86	13.79	μrad (rms)	26.8%	26.6%	$(4\lambda)/(\pi D)$

D defined as aperture diameter.

TABLE 15

4-in Beam Platform Jitter Results

Jitter Conditions	Az	El	Units	Az	El	Units
Applied	278.17	368.53	μrad (rms)	1432.1%	1897.3%	$(4\lambda)/(\pi D)$
Residual	62.90	36.85	μrad (rms)	323.8%	189.7%	$(4\lambda)/(\pi D)$

D defined as aperture diameter.

quad-cell Az output to fluctuate away from the null position at 0 V. The 4-in beam jitter test is not successful with our TFL due to the limitations of the FSM throw (dynamic range).

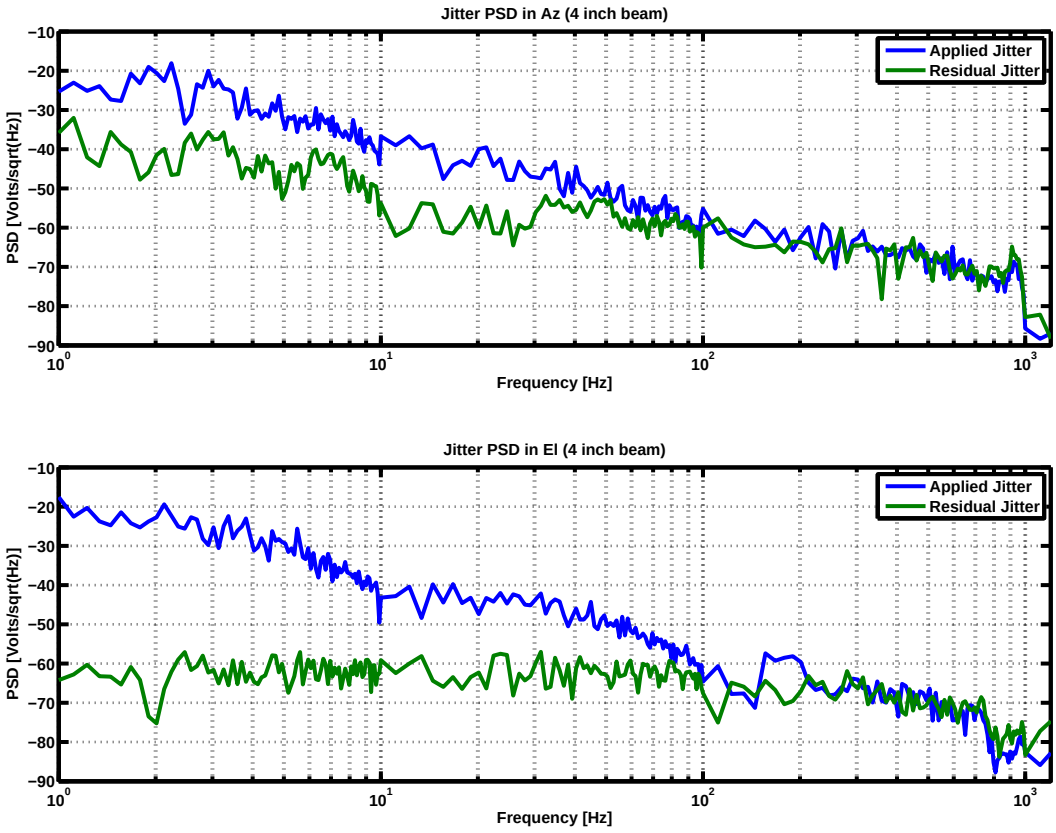

Figure 53. 4-in beam platform jitter PSD.

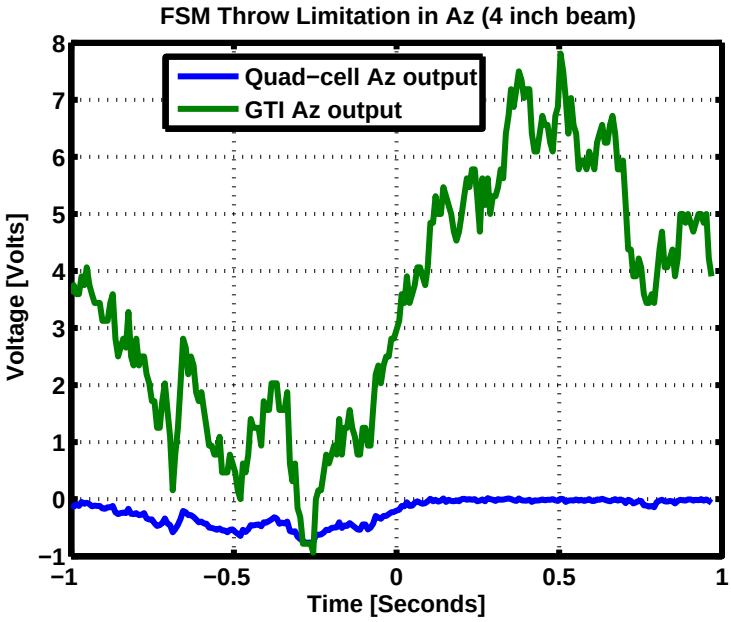

Figure 54. FSM throw limitation for 4-in beam platform jitter.

5. FUTURE WORK

This section provides information on additional tasks that can be done to additionally reduce the size and improve the performance of the compact aircraft lasercom terminal. Future revisions are expected to benefit in performance from implementation of these suggestions.

To further reduce size of the terminal, smaller mounts may be found for the optical components, in particular the quad-cell. Due to the time constraints of the project, we were required to use a larger QC mount than would be necessary. When choosing smaller mounts, caution must be taken in choosing mounts that are small but have a high level of precision and adjustability. The Tx/Rx FLA stages were very compact, however were limited in their ability to adjust along the z-axis. This led to further difficulties in alignment, particularly where focus or beam collimation was important.

Additionally, the Tx FLA would benefit from using an angled connector. A flat connector, as used currently for the Tx FLA, was easier to configure. However, an angled connector should be used to ensure minimal power fluctuations within the terminal. The internal testing of ALT-COM experienced fluctuations due to reflections between the fibers within the terminal.

During construction of the terminal there were difficulties in coupling the beam into the receive fiber. This was due to a lack of independant control of the focus (along the z-axis) on both the Rx FLA and lens mount. Stages that are able to adjust along the z-axis would be especially beneficial in increasing precision. Mounting structures that incorporate an optical ferrule would allow for better control over rotational degrees of freedom than the clamp currently used.

Additionally, with the tracking loop operating, power coupled into the fiber appeared to fluctuate. This was not due to the beam characteristic, but rather misalignment caused by the FSM tracking to the quad cell rather than the FLA. A nutator can be added to the Rx FLA in order to adjust the fiber along with the FSM. This will ensure boresighting for the Rx fiber, minimizing the apparent power fluctuations.

The new FSM was characterized in this project. Its bandwidth was found to be 200 Hz. Testing of the tracking feedback loop showed that the mirror works effectively in the loop at removing platform jitter. This mirror will work sufficiently for lower bandwidth applications. In comparison to the Tracking Testbed FSM with bandwidth 1 kHz, the new FSM bandwidth is rather low. For higher bandwidth applications other FSMs should be investigated. Additionally, it has been suggested that reduction of the mirror size on the current FSM may allow for improvement, however the peak performance of the current FSM is not currently estimated with other mirror sizes. For the 4-in beam platform jitter test, the FSM throw caused limitations in tracking for the azimuth axis. Additional FSMs should be investigated for higher throw.

6. CONCLUSIONS

The design of ALT-COM successfully implemented a piezoelectric stage as well as a new fast-steering mirror. The design was fit on a 12 × 18 in optical breadboard down from 24 × 36 in, a 75% reduction in size. The piezoelectric stage was able to switch between a well-collimated beam for communications, and a divergent beam for acquisition. This is accomplished by moving the stage 400 μm, which was noted to be performed in 9.37 ± 0.77 ms. Polarization maintaining fiber was used in the transmit path to control polarity for successful combination of the transmit and receive paths.

The beam used in ALT-COM was characterized in terms of size, divergence, and wavefront quality. The communication signal was required to be well-collimated resulting in a low divergence. The beam's state as it is emitted from ALT-COM–specifically after the FSM– is characterized in Table 16.

TABLE 16

ALT-COM Beam Characterization

Characteristic	Communication	Beacon
$1/e^2$ Beam Size (mm)	3.8	5.4
$1/e^2$ Beam Divergence (mrad)	0.58	3.02
WaveFront Error (wvs)	0.022	0.560

Optical power of the signal was measured throughout the terminal. Transmission attenuated the signal by (0.33 dB) and reception by (3.7 dB). Coupling into the receive fiber was noted as the highest loss, and dominated in the total losses for the receive path. This excessive loss was due to the difficulty of using an angled fiber which was required to minimize power fluctuations due to feedback. Furthermore, a link budget was developed for this terminal. The link budget suggests that a 2.5 Gb/s link could be supported by ALT-COM and a 40 dBm (10 W) laser source, with a margin of error of 0.47 dB (for reception). This link supposed high altitudes such that complex atmospheric effects can be neglected. It was also noted that transmission for ALT-COM would be more tolerant of error with an error margin of 2.89 dB.

The steering mirrors used in ALT-COM were characterized by various responses in order to understand the entirety of the tracking feedback loop. First of these was a voltage response to examine how angle changed with voltage. The new fast-steering mirror has a mechanical throw of 1500 μrad. Frequency responses were then performed on the mirrors as well as the quad-cell detector in order to determine the bandwidth of the tracking loops. The PI FSM was evaluated to find a bandwidth of 200 Hz. This bandwidth is much less than the FSM used in the Tracking Testbed, however the PI FSM was still used for tracking to evaluate its performance.

For the point-ahead mirror, basic control software was implemented. The software was used to test accuracy of positioning of the PAM. Furthermore, this allowed for running various scan

tests. This included a spiral scan used for acquisition, as well simulating typical aircraft jitter for three beam models (0.5-, 1.5-, and 4-in beams).

The signal to the fast-steering mirror from the quad-cell was properly conditioned to allow for tracking. Part of this required the FSM be properly oriented, as to match the axis of the quad-cell. The gimbal tracking interface circuit was modified in order to increase the integration bandwidth, in turn increasing the bandwidth of the loop to 200 Hz. The tracking feedback loop bandwidth was limited by the bandwidth of the FSM.

The feedback loop was, however, successful in removing platform jitter for both the 0.5- and 1.5-in beam models. In particular, for the 1.5-in beam model, applied jitter 250% of the beamwidth was reduced to 25% of the beamwidth. The FSM, used in the TFL, is effective in removing platform jitter for low bandwidth applications, however the FSM throw causes limitations in Az for the 4-in beam platform jitter test.

The design of ALT-COM makes a successful transition to a path-to-flight design, which has been demonstrated to exhibit acceptable performance for applications requiring a bandwidth of up to 200 Hz. Currently, the major limiting factors in operation are the PI FSM bandwidth and throw as well as coupling into the receive fiber. The FSM may be replaced or alternatively reevaluated with a smaller mirror to increase tracking performance. Comparatively, mounting solutions have been suggested to increase fiber coupling efficiency. Future revisions may take advantage of the noted limitation and move closer to meeting the full design requirements.

REFERENCES

[1] Stephen B. Alexander. *Optical Communication Receiver Design*. SPIE Optical Engineering Press, 1997.

[2] Marcus Borengasser, William Hungate, and Russell Watkins. *Hyperspectral Remote Sensing: Principles and Applications*. Taylor & Francis Series in remote sensing applications. CRC Press, 2008.

[3] Personal communication with Tim Williams, September 2008.

[4] CVI Laser, LLC. *Polarizing Beamsplitter Cubes*, 2007. http://www.cvilaser.com/common/pdfs/PBS.pdf.

[5] Sherman Karp, Robert M. Gagliardi, Steven E. Moran, and Larry B. Stotts. *Optical Channels: Fibers, Clouds, Water, and the atmosphere*. Plenum Press, 1988.

[6] Stephen G. Lambert and William L. Casey. *Laser Communications in Space*, chapter 3, pages 94+. Artech House, Boston, Massachusetts, 1995.

[7] José Miguel López-Higuera. *Handbook of Optical Fibre Sensing Technology*, chapter 5. John Wiley & Sons, New York, New York, 2002.

[8] John E. Mulholland and Sean Anthony Cadogan. Intersatellite laser crosslinks. *IEEE Transactions on Aerospace and Electronic Systems*, 1996.

[9] Richard S. Quimby. *Photonics and Lasers: An Introduction*. John Wiley & Sons, Inc., 2006.

[10] Robert D. Quinnell. Limitations on the use of root-mean-square (rms) phase to describe beam quality characteristics. In Klein, C. A., editor, *Society of Photo-Optical Instrumentation Engineers (SPIE) Conference Series*, volume 293, pages 12–19, Jan 1981.

[11] WaveFront Sciences, Inc. *Complete Light Analysis System 2D*, May 2002.

[12] Dr. Heinz Willebrand and Baksheesh S. Ghuman. *Free-Space Optics: Enabling Optical Connectivity in Today's Networks*, chapter 1. Sams Publishing, Indianapolis, IN, 2002.

[13] James C. Wyant and Katherine Creath. *Basic Wavefront Aberration Theory*, chapter 9, pages 28–39. Academic Press, Inc., 1992.

APPENDIX

6.1 LIST OF ACRONYMS AND ABBREVIATIONS

Table 17
List of Acronyms and Abbreviations

Abbreviation	Description
A/I	Analog Input
A/O	Analog Output
ALT-COM	Aircraft Lasercom Terminal Compact Optical Module
Az	Azimuth
DSA	Dynamic Signal Analyzer
CAD	Computer-Aided Design
DAQ	Data Acquisition Hardware
El	Elevation
FC/PC	Fiber Connector/Physical Contact
FC/APC	Fiber Connector/Angled Physical Contact
FEC	Forward-Error Correction
FLA	Fiber Launch Assembly
FPA	Focal-Plane Array
GUI	Graphical User Interface
GTI	Gimbal Tracking Interface
FSM	Fast Steering Mirror
HW	Half Wave-Plate
HWP	Half Wave-Plate
LED	Light-Emitting Diode
MIT LL	MIT Lincoln Laboratory
NI	National Instruments
PAM	Point-Ahead Mirror
PANDA	Polarization-maintaining and Absorption-reducing
PBS	Polarization Beam-Splitter
PC	Personal Computer
PI	Physik Instrumente
PM	Polarization-Maintaining
PMF	Polarization-Maintaining Fiber
PSD	Power Spectral Density
PXI	PCI eXtensions for Instrumentation
QC	Quad-cell
QW	Quarter Wave-Plate
QWP	Quarter Wave-Plate

Table 17 Continued	
RMS	Root-Mean-Square
Rx	Receive
Std Dev	Standard Deviation
TFL	Tracking Feedback Loop
TT	Tracking Testbed
TTB	Tracking Testbed
Tx	Transmit
VOA	Variable Optical Attenuator
WFS	Wave-Front Sensor

6.2 GIMBAL TRACKING INTERFACE CIRCUIT

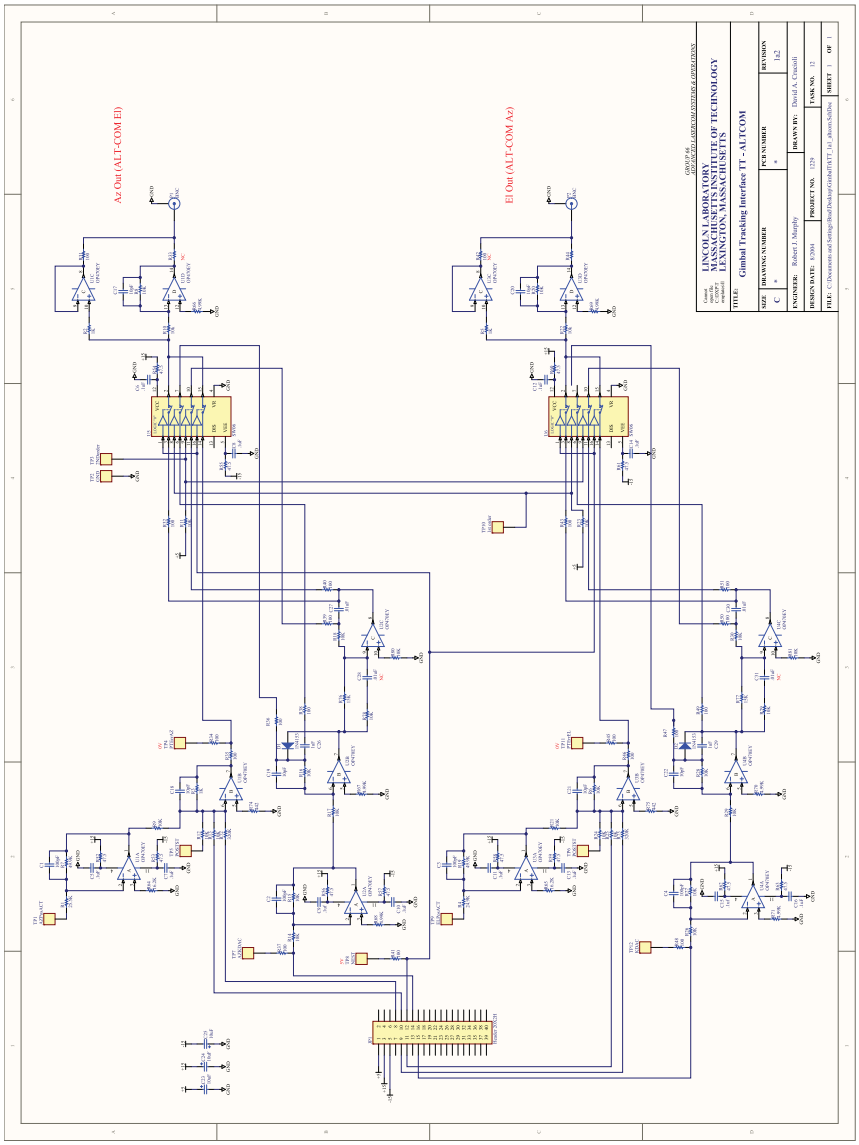

Figure 55. Gimbal tracking interface circuit.